nature materials

REVIEW ARTICLE
PUBLISHED ONLINE: 23 MARCH 2016 | DOI: 10.1038/NMAT4599

Metal oxides for optoelectronic applications

Xinge Yu[1,2], Tobin J. Marks[1*] and Antonio Facchetti[1,3*]

Metal oxides (MOs) are the most abundant materials in the Earth's crust and are ingredients in traditional ceramics. MO semiconductors are strikingly different from conventional inorganic semiconductors such as silicon and III–V compounds with respect to materials design concepts, electronic structure, charge transport mechanisms, defect states, thin-film processing and optoelectronic properties, thereby enabling both conventional and completely new functions. Recently, remarkable advances in MO semiconductors for electronics have been achieved, including the discovery and characterization of new transparent conducting oxides, realization of p-type along with traditional n-type MO semiconductors for transistors, p–n junctions and complementary circuits, formulations for printing MO electronics and, most importantly, commercialization of amorphous oxide semiconductors for flat panel displays. This Review surveys the uniqueness and universality of MOs versus other unconventional electronic materials in terms of materials chemistry and physics, electronic characteristics, thin-film fabrication strategies and selected applications in thin-film transistors, solar cells, diodes and memories.

The discovery of hydrogenated amorphous silicon (a-Si:H) exposed new frontiers in large-area electronics[1]. This semiconductor is a key material for thin-film transistors (TFTs) used in display backplane electronics; yet, its low carrier mobility (~0.5–1.0 $cm^2 V^{-1} s^{-1}$), optical opacity, poor current-carrying capacity and modest mechanical flexibility present challenges for future applications. To overcome such limitations, researchers have explored the use of metal oxides (MOs), which, compared with crystalline silicon and other III–V semiconductors, exhibit unique properties, including excellent carrier mobilities even in the amorphous state, mechanical stress tolerance, compatibility with organic dielectric and photoactive materials, and high optical transparency. Furthermore, high-quality electronic-grade MO thin films are accessible using vapour- and solution-phase methodologies in near-ambient conditions (~25 °C under air), widening their applicability to high-value products such as inexpensive circuits, and to flexible organic light-emitting diode (OLED) displays and solar cells on plastic substrates.

The first MO TFT using semiconducting SnO_2 was reported in 1964 (ref. 2), yet it was the more recent work by Hosono that stimulated extensive research and increases in performance[3]. MO TFTs based on polycrystalline MO materials such as indium oxide (In_2O_3; ref. 4), tin oxide (SnO_2; ref. 5) and zinc oxide (ZnO; ref. 6) were reported. The first amorphous oxide semiconductors (AOSs), whose compatibility with large-area fabrication processes make them technologically appealing, were synthesized in 1954 (ref. 7), yet there was little interest in their properties until Hosono's work on In–Ga–Zn oxide (IGZO) sparked worldwide attention in 2003 (ref. 8). IGZO TFTs have since been commercialized in active-matrix displays, joining the widely used transparent conducting oxide (TCO) electrode material, tin-doped indium oxide (ITO). The unique properties of MOs, their synthesis and their use in optoelectronic devices are described in this Review.

Optoelectronic properties of metal oxides

Carrier mobility is a key metric of semiconductor performance. Traditional band theory descriptions of transport in semiconductors, including wide-gap ionic MOs, represent electronic structure in reciprocal space, with the conduction band minimum (CBM) and the valence band maximum (VBM) curvatures and dispersions determining the electron and hole effective masses, respectively. Smaller effective masses mean greater CBM and VBM hybridization, affording larger carrier mobilities, all other factors being equal. Note that transport in MOs is very different from that in Si semiconductors, where hybridized sp^3 σ-bonding and sp^3 σ*-antibonding states define the VBM and CBM, respectively[9]. In the oxides of interest here, the VB is typically composed of occupied 2*p* O anti-bonding states, and the CB primarily of unoccupied *ns* metal bonding states (Fig. 1a)[8]. The spatially extended, spherically symmetrical *ns*-orbital CBM affords small electron effective masses and efficient electron transport even in the amorphous state, because the spherically symmetrical metal *s*-orbital overlap is minimally affected by lattice distortions. In contrast, the spatially directional Si sp^3 σ states experience dramatically reduced carrier mobilities in the amorphous (a-Si) state. Thus, the electron mobilities of AOSs are often similar to those of the corresponding single crystals[8], and the subgap distributions of the density of states (DOS) between amorphous covalent (such as a-Si) and amorphous oxide (such as a-IGZO) semiconductors differ greatly (Fig. 1b)[9]. The subgap DOS in a-IGZO is 10–100 times smaller than in a-Si:H[10,11].

Many MO (semi)conductors have energy gaps greater than 3 eV, hence, they are transparent in the visible spectrum. Although from a traditional band-structure perspective, high conductivity and optical transparency seem contradictory[12]; in many (semi)conducting MOs, strong interactions between the O 2*p*- and metal *ns*-orbitals produce a band structure characterized by high free-electron mobility (μ_e) due to the low effective mass and by low optical absorption due to the large bandgap (Burstein-Moss shift) and the low DOS in the CB (ref. 12). However, this unique electronic structure causes a dearth of p-type MOs, as hole conduction is hampered by localized O 2*p* orbitals and deep VBM levels where holes are trapped by O ions[12,13]. Band-structure and band-energy modifications are key strategies for the design of p-type MOs, and electrical, X-ray and photoemission experiments argue that greater VBM dispersion is

[1]Department of Chemistry and the Materials Research Center, Northwestern University, 2145 Sheridan Road, Evanston, Illinois 60208, USA. [2]State Key Laboratory of Electronic Thin Films and Integrated Devices, School of Opto-electronic Information, University of Electronic Science and Technology of China (UESTC), Chengdu 610054, China. [3]Polyera Corporation, 8045 Lamon Avenue, Skokie, Illinois 60077, USA. *e-mail: t-marks@northwestern.edu; a-facchetti@northwestern.edu

© 2016 Macmillan Publishers Limited. All rights reserved

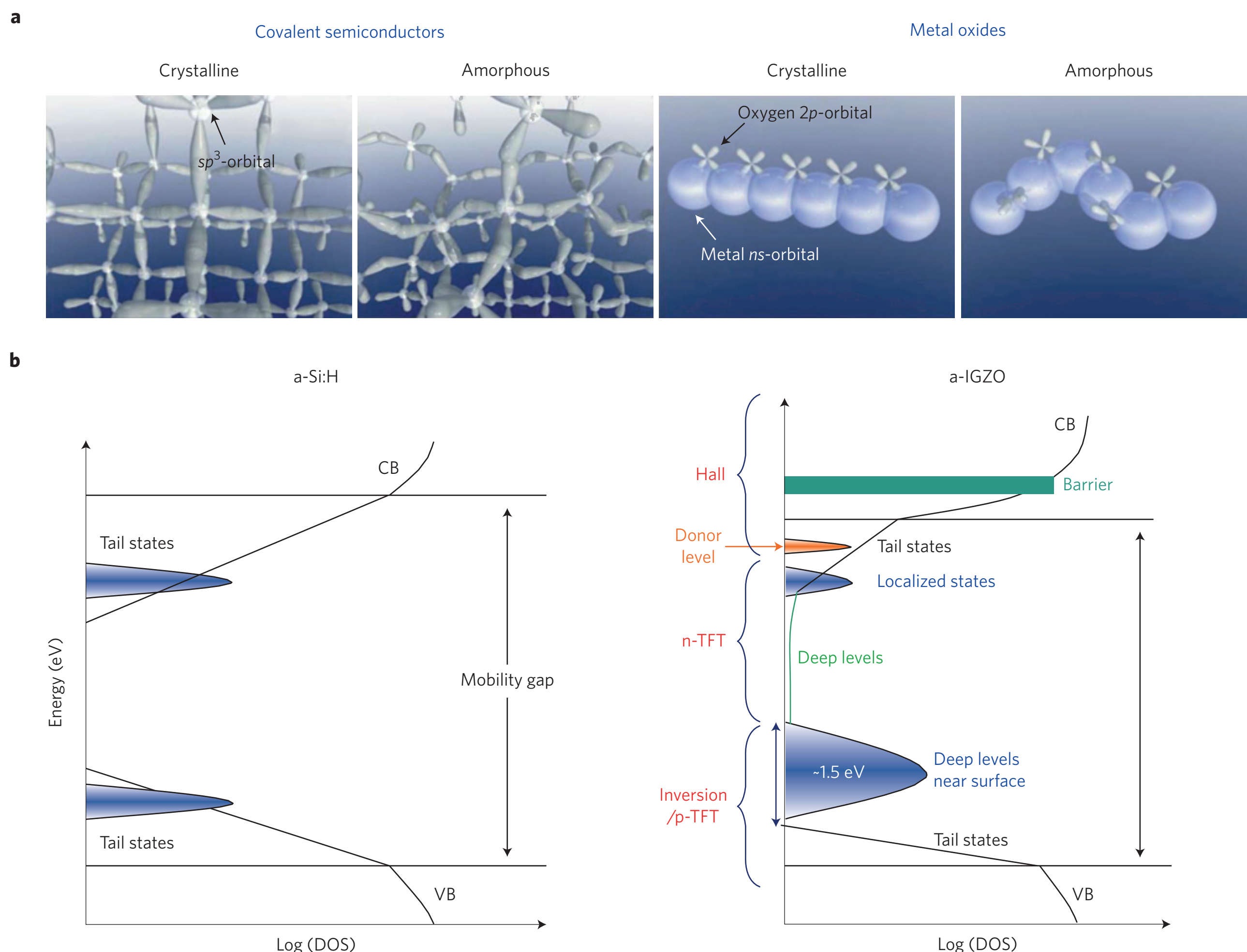

Figure 1 | Electronic structures of Si and metal oxides. a, Schematic orbital contours for charge transport pathways in the conduction band of crystalline and amorphous covalent semiconductors (Si) and metal oxides. **b**, Comparison of subgap DOS in a-Si:H and a-IGZO (different DOS govern n- or p-type TFT behaviours, donor levels and Hall effect parameters; the barrier is the energy distribution when working in percolation conduction). VB, valence band; CB, conduction band. Figures reproduced from: **a**, ref. 8, NPG; **b**, ref. 9, IEEE.

achievable using metal orbitals with energies close to O 2*p* or using more extended anion orbitals, as in $CuGaO_2$ and $SrCu_2O_2$ (ref. 14).

In optoelectronic applications, MO semiconductors compete to some degree with other unconventional semiconductors. The most promising alternatives include organic semiconductors, carbon nanotubes (CNTs), and 2D materials such as graphene and MoS_2 (Table 1). Organic semiconductors, both small molecule and polymer, share a common structural motif of delocalized π-electrons and solubilizing substituents (typically hydrocarbons)[15]. In contrast to MO semiconductors, these organics can efficiently transport holes, electrons or both depending on their structures, and recent advances include very high mobilities, approaching poly-Si. Furthermore, these π-organics are easily solution processed to afford stable formulations and inks, with polymers preferred for printing. However, these organic solids are bound by relatively weak intermolecular interactions, so that post-deposition film processing has stringent process windows to preserve film continuity and morphology. Similar to Si, the largest mobilities are obtained from structures forming uniform, contiguous crystalline domains, with minimum grain boundaries to compromise device metrics and uniformity[16]. Most π-organics exhibit intense optical transitions in the visible, limiting transparency.

Single-wall CNTs (SWCNTs) are seamless single-walled graphene nanocylinders[17] with typical diameters ranging from 0.3 to 70 nm and lengths reaching the centimetre scale. Depending on their chirality (degree of bond connectivity twisting), SWCNTs can be semiconducting or metallic; for instance, the bandgap for ~1-nm-diameter SWCNTs is ~1 eV — similar to that of Si. SWCNTs exhibit extraordinarily high strength and stiffness, and single SWCNTs can have extremely high hole mobilities (μ_h) and conductivities. However, these parameters fall significantly in SWCNT network films. Single-tube and CNT network-based devices can be fabricated either by vapour phase (typically chemical vapour deposition, CVD) or solution phase (typically spin-coating) processes. Metallic SWCNT films are now commercially available as viable alternatives to metals and MOs, whereas the use of semiconducting SWCNTs is more limited by process reliability, cost and film performance stability.

Graphene is another promising electronic material consisting of sp^2 carbon atom monolayers with a 2D honeycomb lattice[18]. Single graphene layers are obtained from graphite by simple mechanical exfoliation, and CVD processes can also be utilized for their synthesis. As for SWCNTs, graphene also exhibits impressive mechanical stiffness. Graphene is a gapless semiconductor with high μ_e and electrical conductivity. However, lack of reliable and cost-efficient production of perfectly structured graphene and the gapless electronic structure have to date limited large-scale implementation. Two-dimensional layered transition metal dichalcogenides, especially MoS_2, have also advanced rapidly[19]. MoS_2 monolayers not only exhibit good chemical stability, but also unique mechanical and electrical properties

© 2016 Macmillan Publishers Limited. All rights reserved

Table 1 | Comparative metal oxide, silicon, organic, single-wall carbon nanotubes, graphene and MoS_2 semiconductor optoelectronic properties.

Material	Polarity	Bandgap (eV)	Typical growth methods	μ_e or μ_h ($cm^2 V^{-1} s^{-1}$)	Transport type	Ref.
Metal oxide	p, n*	2.0–8.0	Sputtering, PLD, thermal evaporation, spin-coating, printing	10^1–10^2 (single crystal, by vapour phase) 10^{-3}–10^1 (polycrystal or amorphous, by vapour phase, solution)	Band-like	12
Silicon	p, n	~1.1	CVD, liquid-phase epitaxy, spin-coating, printing	10^2–10^3 (single crystal) 10^1–10^2 (polycrystal) 10^{-1}–10^0 (amorphous) 10^{-1}–10^2 (solution)	Band-like (crystalline) Band-like or hopping (amorphous)	8
Organic small molecules	p*, n	2.5–4.0	Thermal evaporation, spin-coating, printing	10^0–10^1 (single crystal) 10^{-5}–10^1 (v) 10^{-5}–10^1 (SC) 10^{-4}–10^1 (Pr)	Band-like (single crystal) MTR (polycrystalline) VRH (amorphous)	15
Organic polymers	p*, n	1.5–2.5	Spin-coating, printing	10^{-5}–10^1 (SC) 10^{-5}–10^0 (Pr)	MTR (polycrystalline) VRH (amorphous)	15
Single-wall carbon nanotubes	p*, n	~1.0	CVD, spin-coating, printing	10^6 (maximum, single tube) 10^1–10^4 (CVD) 10^{-1}–10^2 (SC) 10^{-1}–10^2 (Pr)	Ballistic (single tube) Percolating in network (carbon nanotube films)	17
Graphene	n, p*	Absence of bandgap	CVD, micromechanical exfoliating, spin-coating, printing	10^5 (maximum, single sheet) 10^1–10^4 (CVD) 10^1–10^4 (ME) 10^{-1}–10^2 (SC) 10^{-1}–10^2 (Pr)	Ballistic (single flake) Percolation (graphene films)	18
MoS_2	n, p*	1.3–1.8	CVD, micromechanical exfoliating, spin-coating, printing	10^3 (maximum, single sheet) 10^1–10^2 (CVD) 10^0–10^2 (ME) 10^0–10^2 (Pr)	Band-like	19

*Predominant character. MTR, multiple trapping and release; VRH, variable range hopping; v, vapour phase; SC, spin-coating; Pr, printing; ME, mechanically exfoliated.

approaching high-quality graphene sheets, but with a semiconducting gap. MoS_2 monolayers can be obtained by micromechanically exfoliating bulk MoS_2 crystals, CVD growth, or solution processing and post-annealing. Nevertheless, uniform growth of large-area, high-quality MoS_2 thin films remains challenging.

With respect to these materials, MOs (and AOSs in particular) still present clear advantages for optoelectronic applications as a result of the combination of high carrier mobility, good optical transparency, straightforward synthetic access, large-area electrical uniformity and mechanical flexibility. In the following sections, we focus on MO applications in TFTs (Table 2), diodes, memories and photovoltaics (Table 3), subdividing the TFT section according to their growth methodology (detailed in Box 1).

Vapour-processed transistors

TFTs are 'valves' in which charge transport is modulated by applying two independent electrical potentials (Fig. 2a). These three-terminal devices have a conducting gate, source and drain electrodes contacting a semiconductor, and a dielectric insulator layer between the semiconductor and the gate electrode. Charge carriers accumulate under a gate voltage bias, and drift from the source to drain electrode. The source–drain current scales as the carrier density multiplied by the carrier mobility (μ), the most significant metric in TFTs, and constrains the device operational speed. The current on/off ratio, $I_{on/off}$, the threshold voltage (V_T) and bias stability are additional important TFT metrics. For TFT fabrication, the semiconductor channel layer, the source–drain electrodes and the gate insulator layer are deposited using either vapour-phase or solution methods (Box 1). Although we focus here on MO semiconductors (Table 2), MOs with more conducting or insulating character can also be implemented in every TFT component, including the gate, source and drain electrodes, and the gate dielectrics.

SnO_2 (ref. 2) and In_2O_3 (ref. 20) films fabricated by thermal evaporation and sputtering, respectively, were the first MO semiconductors used in TFTs, yet they exhibited modest performance (Table 2). In contrast, the enhanced crystallinity of ZnO films grown by radiofrequency magnetron sputtering at 25 °C allowed μ_e of about 1.2 $cm^2 V^{-1} s^{-1}$ to be reached[21], further improved to $\mu_e \geq 50$ $cm^2 V^{-1} s^{-1}$ by using gate insulators with a high dielectric constant k (ref. 22). In fact, it has been shown that mobility in MOs displays a power law dependence on k (ref. 23). Recently, flexible ZnO TFTs with $\mu_e \approx 20$ $cm^2 V^{-1} s^{-1}$ have been fabricated using atomic layer deposition (ALD) at 90 °C (ref. 24).

Despite these encouraging results, carrier density in MOs is difficult to control owing to large numbers of oxygen vacancies[25,26]; major advances were achieved when Hosono and colleagues synthesized IGZO films grown epitaxially on single-crystal yttria-stabilized zirconia substrates[3]. High-resolution cross-sectional transmission electron microscopy indicates that the $InGaO_3(ZnO)_5$ lattice has alternating InO_2 and $GaO(ZnO)_5$ layers stacked along the (0001) direction, similar to ITO and Ga-doped ZnO (Fig. 2b). The film/substrate interface is atomically flat despite the high-temperature annealing (1,400 °C), with the lattice mismatch relaxed within a few atomic layers from the interface. Importantly for carrier stabilization, introducing Ga in the $GaO(ZnO)_5$ layers does not generate carriers as it not only replaces Zn^{2+} in the tetrahedral sites, but also occupies trigonal-bipyramidal coordination sites, thereby maintaining local electroneutrality. The InO_2 layers prevent O_2 out-diffusion, which would create carrier-generating O vacancies. IGZO TFTs fabricated using ITO source, drain and gate contacts, and an amorphous HfO_2 dielectric exhibited $\mu_e = 80$ $cm^2 V^{-1} s^{-1}$ and $I_{on/off} = 10^6$.

This excellent performance encouraged the exploration of IGZO AOSs, and transparent a-IGZO TFTs were fabricated on plastic substrates[8]. a-IGZO films were deposited at 25 °C by pulsed-laser

© 2016 Macmillan Publishers Limited. All rights reserved

Table 2 | Thin-film transistor metrics for representative vapour- and solution-processed metal oxide semiconductor films.

Deposition technique	Metal oxide	Polarity	Source-drain/ gate	Dielectric	Substrate	μ_e or μ_h ($cm^2 V^{-1} s^{-1}$)	$I_{on/off}$	T_{growth}/T_a (°C)	Year	Ref.
Vapour phase										
Thermal	SnO_2	n	Al	Al_2O_3	Glass	NA	NA	-	1964	2
PLD	IGZO	n	ITO/ITO	Y_2O_3	PET	7	10^3	RT/NA	2004	8
ALD	ZnO	n	Au/ITO	AHO	PET	20.2	10^7	90/NA	2015	24
Sputtering	ZnO	n	Ti/Au/Si	SiO_2	Si	1.2	10^6	RT/NA	2003	21
	In_2O_3	n	ITO/Si	SiO_2	Si	15.3	10^8	RT/NA	2010	26
	IGZO	n	Au/Si	SiO_2	Si	73.9	10^7	RT/150	2009	33
	IZO	n	ITO/Si	SiO_2	Si	30.4	10^8	RT/200 (O_2)	2013	25
	IGZO	n	Mo	SiN_x/SiO_2	Glass	6.7	10^9	RT/300	2015	32
	SnO	p	Au/Ti	Al_2O_3	ZrO_2	1.3	10^2	500/NA	2008	34
	SnO	p	Ni/Au/IZO	Paper	Paper	1.3	10^2	RT/150	2013	35
	CuO_x	p	Au/ITO	ATO	Glass	0.01	10^4	RT/NA	2014	38
Sol–gel chemistry										
Spin-coating	In_2O_3	n	Au/Si	SiO_2 (SAND)	Si	0.7 (43.7)	10^6	400/NA	2008	43
	ZnO	n	Zn/ITO	ATO	Si	5.25	10^5	500/NA	2007	41
	IZO	n	W/Si	SiO_2	Si	11.4	10^8	250/NA	2011	47
	IGZO	n	IZO/Ti/Au	Al_2O_3	PAR	3.77	10^8	RT/NA	2012	49
	IZO	n	ITO/ITO	Al_2O_3	Polyimide	4.03	10^9	250/NA	2013	46
	ZnO	n	Al/Si	SiO_2	Si	10	10^7	180/NA	2013	42
	IGZO	n	Al/Si	SiO_2	Si	10.1	10^5	400/NA	2013	48
	QSL	n	Al/Al	Al_2O_3/ZrO_2	Glass	40	10^4	200/NA	2015	50
	CuO_x	p	Ni	SiO_2	Si	0.29	10^4	700 (vacuum)/NA	2015	59
Ink jet	IGZO	n	Ti/Au/Si	SiO_2	Si	10.5	10^5	Light irradiation	2015	54
Gravure	IGZO	n	Mo/Ti	SiN_x	Glass	0.81	10^6	550/NA	2010	55
	In_2O_3	n	Al/Au	Al_2O_3	PI	8	10^6	300/150	2015	56
	IZO	n	ITO/Si	SiO_2	Si	9.1	10^6	425/NA	2015	57
Aerosol-jet printing	ZnO	n	Au/Cr/ PEDOT:PSS	Ion-gel electrolyte	Kapton	1.6	10^5	250/NA	2013	58
Spray pyrolysis										
Spray	ZnO	n	Al/Si(Al/Al)	SiO_2 (SAM)	Si	15 (7.6)	10^6 (10^3)	400/NA	2009	60
	CuO_x	p	ITO/Au/Si	SiO_2	Si	10^{-3}	10^3	275/NA	2013	61
Combustion										
Spin-coating	In_2O_3	n	Al/Al	Al_2O_3	AryLite	6.0	10^3	200/NA	2011	62
	IYO	n	Al/Si	Zr-SAND	Si	5.0	10^5	250/NA	2012	63
	IYZO	n	Al/Si	SiO_2	Si	2.37	10^7	300/NA	2013	65
	IGZO	n	Al/MoW	SiO_2	Glass	1.4	10^6	350/NA	2013	64
	IGZO	n	Al/Si	SiO_2	Si	5.43	10^8	300/NA	2013	65
	ILO	n	Al/Si	SiO_2	Si	9.7	10^7	300/NA	2015	66
Spray	In_2O_3	n	Al/Al	Al_2O_3	AryLite	11.0	10^4	200/NA	2015	68
	IGZO	n	Al/Si	SiO_2	Si	7.53	10^7	300/NA	2015	68
Pre-formed nanostructures	ZnO	n	ITO/IZO	Al_2O_3	Glass	96	10^6	Thermal growth	2007	72
	CuO_x	p	Au/Si	SiO_2	Si	15	10^2	500/NA	2009	73
	ZnO	n	Al/Si	SiO_2	Si	1.75	10^8	250/NA	2013	76

ATO, antimony tin oxide; AHO, aluminum hafnium oxide; T_{growth}, film growth temperature; T_a, post film-deposition annealing temperature; NA, not applicable or not reported; QSL, quasi-superlattices of structure In_2O_3–Ga_2O_3–ZnO–Ga_2O_3–In_2O_3; SAM, self-assembled monolayer; RT, room temperature; IYZO, indium yttrium zinc oxide; ILO, indium lanthanum oxide; SAND, self-assembled nanodielectric; PAR, polyarylate.

deposition (PLD) using a polycrystalline $InGaZnO_4$ target, yielding a In:Ga:Zn = 1.1:1.1:0.9 elemental composition. These films are stable up to 500 °C in air and have an optical bandgap of 3.0 eV — similar to crystalline IGZO (3.4 eV). The a-IGZO carrier concentration is tunable from 10^{14} to 10^{20} cm^{-3} by varying O_2 partial pressure from 7 to 0.1 Pa (Fig. 2c). The Hall mobility of amorphous and crystalline IGZO film depends on carrier concentration, and the two values converge to ~10 $cm^2 V^{-1} s^{-1}$ at high carrier densities. Mechanically flexible a-IGZO TFTs on polyethylene terephthalate (PET) achieved μ_e = 6–9 $cm^2 V^{-1} s^{-1}$.

The use of radiofrequency sputtering to fabricate a-IGZO TFTs has allowed the intrinsic limitations of PLD in terms of area

© 2016 Macmillan Publishers Limited. All rights reserved

Table 3 | Applications of representative metal oxide materials in microelectronics, including transparent conducting oxides, diodes, random access memories, solar cells and organic photovoltaics.

Application	Metal oxide	Deposition technique	Performance parameters	Processing temperature (°C)	Year	Ref.
p–n junction						
Diodes	$CuCrO_2$:Mg–ZnO	PLD	I_D = 7 mA (2 V)	RT (laser annealing)	2008	80
Sensors	WO_3–SnO_2	Sol–gel	NO_2 200 ppm	200	2010	82
	ZnO–SnO_2	Sol–gel	C_2H_5OH 200 ppm	300	2007	85
	ZnO–SnO_2	PECVD	CO 100 ppm	350	2011	84
Solar cells	Ga_2O_3–Cu_2O	PLD	PCE = 5.38%	RT	2013	88
	Cu_2O–TiO_2–ZnO (nanowire)	Vapour + ALD	PCE = 0.39%	1,140 (HP O_2)	2014	89
Random access memories	Cu_xO	ECP	$R_{HS}/R_{LS} = 10^3$	NA	2009	91
	ZrO_2	Sol–gel	$R_{HS}/R_{LS} = 10^2$	600	2009	93
	NiO	Sputtering	$R_{HS}/R_{LS} = 10^3$	300	2009	92
Transparent conducting oxides	ITO	Sputtering	$\rho = 10^{-4}$ Ω cm	RT	2010	12
	AZO	Sputtering	$\rho = 10^{-4}$ Ω cm	RT	2010	12
	IZO	Sputtering	$\rho = 10^{-4}$ Ω cm	RT	2010	12
	GZO	Sputtering	$\rho = 10^{-4}$ Ω cm	RT	2010	12
	ZITO	Sputtering	$\rho = 10^{-4}$ Ω cm	RT	2010	12
Organic photovoltaics						
Electrode	ITO	Commercial	R_s = 5 Ω sq.$^{-1}$, PCE = 0.39%	NA	2013	103
	InCdO–ITO	IAD	R_s = 4.9 Ω sq.$^{-1}$, PCE = 1.14%	RT	2010	105
	ZITO	PLD	R_s = 17.5 Ω sq.$^{-1}$, PCE = 7.41%	RT	2014	106
Interfacial layer	MoO_3	Thermal evaporated	PCE = 3.33%	NA	2006	111
	V_2O_5	Thermal evaporated	PCE = 3.10%	NA	2006	111
	ZnO	Sol–gel	PCE = 10.6%	150	2013	77
	NiO	PLD	PCE = 5.16%	RT	2008	107
	TiO_x	Sol–gel	PCE = 4.1%	150	2007	124

GZO, gallium-doped zinc oxide; I_D, drain current; ρ, resistivity; AZO, aluminum zinc oxide; PECVD, plasma-enhanced chemical vapour deposition; ECP, electrochemical plating; IAD, ion-assisted deposition; HP, high pressure; R_{HS}, high resistance state; R_{LS}, low resistance state. See the main text and Table 2 for other definitions.

deposition to be overcome[27]. Additional device issues, such as bias stress stability, light sensitivity and long-term operational stability, were addressed by post-deposition and fabrication thermal annealing[28], encapsulation[29] and plasma treatment[30]. According to DOS modeling[31], these processes suppress charge trap densities in a-IGZO, especially tail states near the CBM, thereby enhancing stability. Furthermore, exposing the source and drain contact areas of sputtered a-IGZO films to ultraviolet irradiation dramatically reduces the contact resistivity from 10^6 to 10^{-5} Ωcm (ref. 32). Nowadays, sputtering is the preferred industrial process for a-IGZO growth in TFTs for OLED display backplanes. By controlling the process parameters, including O_2 partial pressure, growth pressure, target composition, film thickness and annealing temperature, a-IGZO TFTs processed at 150 °C achieve μ_e = 73.9 cm^2 V^{-1} s^{-1} (ref. 33). Beyond a-IGZO TFTs, other MOs are also being investigated (Table 2), aiming at achieving the stability and performance of a-IGZO with simpler compositions.

All the aforementioned oxides are n-type semiconductors. To date, few p-type MOs have been reported as a result of the aforementioned localized O 2*p*-dominated VB and high densities of deep traps near the VB. Epitaxial SnO_x on (001) yttria-stabilized zirconia at 500 °C yielded the first p-type oxide TFT exhibiting $\mu_h \approx 1.3$ cm^2 V^{-1} s^{-1} (ref. 34). SnO_x p-type TFTs sputtered on paper substrates at 150 °C also afford $\mu_h > 1$ cm^2 V^{-1} s^{-1} (ref. 35), which were combined with n-type a-IGZO TFTs to demonstrate CMOS (complementary metal-oxide semiconductor) differential amplifiers (gain ~4.1 V/V), common source amplifiers (gain ~16.3 V/V) and inverters (gain ~4.9 V/V). Besides SnO_x, CuO_x is interesting due to its high Hall μ_h; ~100 cm^2 V^{-1} s^{-1} was achieved because the tetrahedral coordination of oxide ions in CuO_2 reduces the localization of the O 2*p*-dominated VB. However, obtaining high-performance CuO_x TFTs remains challenging, due to large hole effective masses and deep VBM levels, and difficulties in controlling hole densities. Thus, although high-quality CuO_x films can be grown by PLD on MgO at 850 °C, the resulting TFTs exhibit μ_h of only 0.26 cm^2 V^{-1} s^{-1} (ref. 36). Low-temperature CuO_x sputtering deposition followed by slow post-annealing at 200 °C yielded high film crystallinity, yet the TFT performance remained poor ($\mu_h \approx 10^{-3}$ cm^2 V^{-1} s^{-1})[37]. More recently, transparent p-type TFTs were fabricated on glass substrates using CuO_x films sputtered at 25 °C with $\mu_h \approx 0.01$ cm^2 V^{-1} s^{-1} (ref. 38). These data show that useful MO μ_h values are far from being achieved yet.

Solution-processed transistors

Transitioning film growth from capital-intensive vapour-phase to solution-phase technologies is of paramount importance for MO optoelectronics. Indeed, the possibility of fabricating films from liquid precursors in ambient conditions holds great attraction for MOs versus Si, nitride and chalcogenide semiconductors. Progress here has been impressive (Table 2), opening possibilities for MO printing.

Sol–gel. In typical sol–gel processes, MO precursor solutions are prepared by dissolving metal salts in a solvent, typically H_2O with a 'stabilizing agent'[39]. The resulting coordinated metal species undergo

© 2016 Macmillan Publishers Limited. All rights reserved

Box 1 | Oxide growth techniques.

Metal oxides films can be deposited using vapour- and solution-phase techniques[12,13] as summarized below.

Vapour-phase processing. There are four main vapour-phase techniques for depositing MO films.

Thermal deposition. Thermal evaporation uses a volatile source material under high vacuum to grow films on a substrate of interest, and is widely used to manufacture metallized products. MO film thermal deposition faces several challenges, including: (i) post-deposition O content adjustment is required to achieve the desired composition, owing to O_2 loss during MO evaporation; and (ii) high substrate temperatures are necessary to optimize reactions between ionized species on the substrate, and common plastic substrates are not compatible with high growth rates.

Sputtering. Sputtering is a common technique for depositing MO (semi)conductors. Most utilized is magnetron sputtering where magnets behind the target enhance bombardment by ionized gases, increasing growth rate and film uniformity. Advantages of sputtering include: (i) film growth near room temperature; (ii) compatibility with thermally sensitive substrates, such as plastic foils; and (iii) control of MO film morphology, composition and carrier concentration via the deposition parameters, such as O_2 pressure and sputtering power. Sputtering is widely used industrially for metal and MO depositions. Nevertheless, it is costly due to the specialized equipment and targets, especially for large-area growth.

Pulsed-laser deposition. PLD is also an efficient flash-evaporation technique where a MO or other target is irradiated with a high-power pulsed ultraviolet laser beam, vapourizing the target material in a plasma plume and depositing it as a thin film. This process can occur in vacuum or in a background gas, such as O_2, which is commonly employed in MO film growth. PLD affords high-quality and high-performance films with well-controlled compositions and morphologies. However, it is seldom applicable to production scales because of limitations in large-area film uniformity, low deposition rates and high capital costs.

Atomic layer deposition. ALD films are grown by exposing the substrate to alternating pulses of gaseous reagents that undergo self-limiting chemical reactions. In contrast to chemical vapour deposition, the reagents are never present simultaneously in the reactor, but are inserted as a series of sequential, non-overlapping pulses, resulting in atomic-scale growth. Varying the cycle number enables uniform growth with high precision on arbitrarily complex and large-area substrates. ALD processes are typically used to manufacture high-quality MO dielectric films.

Solution-phase processing. There are three main solution-phase techniques for depositing MO films.

Spin-coating. Spin-coating is a simple method for depositing optoelectronic films, generally on planar substrates. A precursor solution is applied on the substrate surface, fixed by suction to a holder, which is either spinning at low speed or stationary. Next, the substrate is rotated at high speed to spread the coating material by centrifugal force, coating the substrate with a thin film. Film thickness and quality depend on the acceleration and spinning speed as well as the solution and solvent viscosity, volatility and concentration. Spin-coating is widely used in oxide film microfabrication using sol–gel precursors and in integrated circuit fabrication to deposit photoresist layers.

Spray coating. Also known as spray pyrolysis, spray coating is another simple, inexpensive deposition method for electronic materials, compatible with large-area growth on plastic. Films are typically grown by aerosol spraying precursor solutions onto preheated substrates, where the constituents undergo chemical reaction. These chemical reagents are selected such that all reaction products are volatile at the deposition temperature. Spray pyrolysis is particularly useful for MO depositions, and is a commercial method for fabricating transparent electrical conductors on glass. Spray pyrolysis film roughnesses are typically inferior to those of spin-coated films, but can be optimized by adjusting process parameters. Spray pyrolysis requires low viscosity solutions, which restricts the solvent selection.

Printing. Printing is an additive process involving simultaneous film deposition and patterning, typically at low temperatures, thereby minimizing chemical and energy consumption. Furthermore, printed pattern shapes and sizes can be readily modified without process redesign. The most utilized electronics printing techniques are ink-jet, aerosol jet, gravure, flexo and screen printing; note that screen printing is used industrially to create metal lines. Impressive advances have been made in printing organic and MO electronic materials; however, implementation issues at the industrial scale include enhancing formulation stability, broadening process windows, and enhancing film uniformity. Furthermore, for applications such as circuits, resolution and registration must achieve acceptable yields in production. For MOs, high-temperature post-annealing is typically required.

hydrolysis forming hydroxides, which slowly convert to colloidal solutions (sol), and eventually to integrated MO networks (gel) containing liquid and solid phases. For TFTs, films are cast from the sol precursors, which are then thermally annealed to condense the lattice and remove volatile organics. TFTs using MO films — including In_2O_3, IGZO, zinc tin oxide (ZTO), indium gallium oxide (IGO), indium zinc oxide (IZO), and ZnO semiconductors, Al_2O_3, ZrO_2, HfO_2, Ta_2O_5, Y_2O_3 dielectrics, and ITO, In_2O_3 and F-doped ITO conductors — have been fabricated by sol–gel processing.

Among MO TFT semiconductors, sol–gel ZnO TFTs were first fabricated by dip-coating Si or SiO_2 substrates in zinc acetate–propanol or diethanolamine solutions, followed by 900 °C annealing[40]. The resulting devices exhibited $I_{on/off} \approx 10^3$ and transconductance $g_m \approx 0.6$ μS, with no other TFT metrics reported. To lower the processing temperature, the same precursor solutions were used for spin-coated ZnO films, which were then post-annealed at 500 °C. Remarkable μ_e up to 5.25 cm^2 V^{-1} s^{-1} with $I_{on/off} = 10^5$ was achieved with Al–Ti oxide dielectrics and vacuum-deposited Zn contacts[41]. Subsequently, ammonia-based carbon-free precursor solutions yielded ZnO TFTs with a $\mu_e \approx 11$ cm^2 V^{-1} s^{-1} with 180 °C processing[42].

Although less crystallizable than ZnO, In_2O_3 is an ideal sol–gel TFT candidate, and In_2O_3 film growth was achieved by spin-coating solutions of ethanolamine (EAA) and $InCl_3$ in methoxyethanol, varying the EAA:In^{3+} ratio from 0.0 to 15 (Fig. 3a)[43]. EAA strongly affects crystallization, with optimal performance (μ_e = 43.7 cm^2 V^{-1} s^{-1}) achieved for EAA:In^{3+} = 10 and T_{al} = 400 °C. The post-deposition temperature for sol–gel MO films can be

© 2016 Macmillan Publishers Limited. All rights reserved

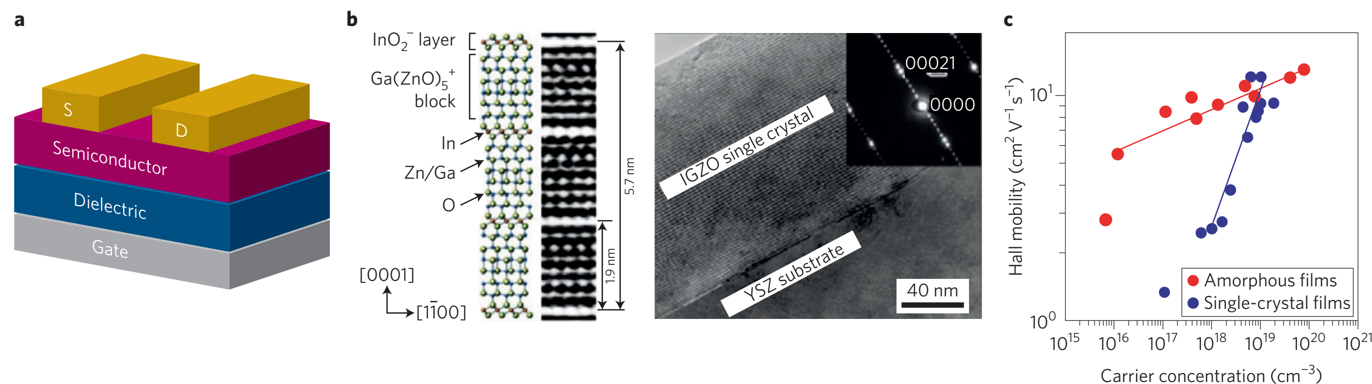

Figure 2 | Vapour-phased metal oxide and thin-film transistor. a, Device architecture of a bottom-gate top-contact thin-film transistor. S, source electrode; D, drain electrode. **b**, Crystal structure schematic (left) and high-resolution transmission electron microscopy lattice image (right) of $InGaO_3(ZnO)_5$. YSZ, yttria-stabilized zirconia. **c**, Plot showing the relationship between 25 °C Hall mobility and carrier concentration for a-IGZO films versus single-crystal $InGaO_3(ZnO)_5$ films. Figures reproduced from: **b**, ref. 3, AAAS; **c**, ref. 8, NPG.

reduced by modifying the thermal treatment conditions (performed under O_3 (ref. 44), with controlled O_2 pressure[45] or in vacuum[46]) or with specialized precursors. For instance, it has been suggested that additional vacuum annealing at 5×10^{-2} Torr and at temperatures lower than 200 °C facilitates In_2O_3 sol–gel condensation, achieving $\mu_e \approx 2.62$ cm^2 V^{-1} s^{-1} (ref. 46).

As with vapour deposition, binary and ternary MO solution processing was also explored. A low-temperature 'sol–gel on chip' route to a-IZO and a-IGZO TFTs (Fig. 3b) was recently demonstrated, where an In alkoxide cluster, $Zn(OCH_2CH_2OCH_3)_2$, and $Ga(OCH(CH_3)_2)_3$ in methoxyisopropanol + 2-methoxyethanol were spin-coated and annealed under controlled humidity to enhance hydrolytic film densification[47]. Amorphous, high-mobility films were optimized using a In/Zn ratio of 7:3 (Fig. 3c). The effects of processing atmosphere (dry or wet) and annealing temperatures were also explored, revealing that wet annealing afforded the highest mobilities (μ_e = 7–12 cm^2 V^{-1} s^{-1} on SiO_2), near-0.0 V turn-on voltages and minimal hysteresis (<1.2 V). a-IGZO TFTs with low Ga content (5%) annealed at 275 °C also afforded good performance with μ_e = 4.05–6.12 cm^2 V^{-1} s^{-1}, although such devices were operationally unstable due to the incomplete hydrolysis of the Ga alkoxide precursor. More recently, formamide incorporation (0–100 vol%) in IGZO precursor solutions yielded a higher a-IGZO TFT μ_e, ~10.1 cm^2 V^{-1} s^{-1} on SiO_2 and 50 cm^2 V^{-1} s^{-1} on high-k aluminum zirconia oxide (AZO) at an annealing temperature of 400 °C (ref. 48).

To further lower the annealing temperatures, precursor decomposition at ~25 °C by deep-ultraviolet irradiation of the deposited MO films was investigated[49]. Exposure under N_2 to deep-ultraviolet light promoted M-O-M lattice densification in IGZO films prepared using a $Zn(C_2H_3O_2)_2$ + $In(NO_3)_3$, + $Ga(NO_3)_3$ solution, and composition and microstructure comparable to 350 °C annealed films were obtained. This approach was used to fabricate a-IGZO TFTs on plastic substrates (Fig. 3f) with μ_e as high as ~7 cm^2 V^{-1} s^{-1}. Positive-gate-bias TFT stress tests show excellent operational stability without film passivation, and a small V_T shift of 1.12 V after 10,000 s gate-bias.

Metal-oxide heterostructures combining two or more MO layers have been recently implemented in TFTs. Unlike conventional single-channel-layer MO TFTs, these TFTs used spin-coated In_2O_3–Ga_2O_3–ZnO–Ga_2O_3–In_2O_3 quasi-superlattices (QSLs)[50]. The performance of these transistors is not limited by the individual semiconductor bulk carrier mobilities, but is instead dominated by the heterointerface structural and electronic properties within the QSL. QSL TFTs processed at 200 °C show μ_e > 40 cm^2 V^{-1} s^{-1}, far exceeding those of single-layer devices.

Sol–gel methods are particularly attractive for their compatibility with printing processes for the fabrication of MO TFTs and other optoelectronic devices[51,52]. The first ink-jet printed IZO TFT was achieved[53] using aqueous $InCl_3$ + $ZnCl_2$ solutions printed on Si–SiO_2 substrates, reaching μ_e = 7.4 cm^2 V^{-1} s^{-1} after 400 °C annealing. Recently, ink-jet printed a-IGZO TFTs, with $\mu_e \approx$ 10.1 cm^2 V^{-1} s^{-1} after intense pulsed white light irradiation (100 J cm^{-2}) were demonstrated[54]. Gravure printing of $Zn(C_2H_3O_2)_2$, $In(NO_3)_3$ and $Ga(NO_3)_3$ inks was also used to fabricate a-IGZO TFTs exhibiting μ_e = 0.81 cm^2 V^{-1} s^{-1} after 550 °C annealing[55]. Recently, gravure- and flexo-printing In_2O_3 (using $In(NO_3)_3$ precursor ink), and a-IZO (using $In(C_4H_6NO_3)_3$+ $Zn(C_4H_6NO_3)_2$ inks) TFTs were also demonstrated, with μ_e = 8 cm^2 V^{-1} s^{-1} after 300 °C annealing[56], and μ_e = 9.1 cm^2 V^{-1} s^{-1} after 425 °C annealing, respectively[57]. Note that the ultrahigh capacitance and compatibility with printing processes of ion–gel electrolytes make them good candidates as dielectrics for low-voltage MO TFTs. Thus, aerosol-jet TFT printing of semiconducting ZnO ($Zn(NO_3)_2$ precursor ink) and electrolyte dielectrics afforded μ_e = 1.6 cm^2 V^{-1} s^{-1} after 250 °C annealing[58]. However, high-temperature annealing (500 °C) leads to significantly better performance (μ_e = 12.9 cm^2 V^{-1} s^{-1}) for all-printed a-IZO TFTs[59];,hence, further work is needed to make this technology compatible with inexpensive plastic substrates.

The availability of sol–gel p-type MOs has lagged far behind n-type MOs. To our knowledge, the first p-type sol–gel Cu_2O TFT was only recently achieved, with μ_h = 0.16 cm^2 V^{-1} s^{-1} obtained using a $Cu(OAc)_2$ precursor solution and a two-step 700 °C annealing process, first under N_2 then under O_2, which is essential for optimum film morphology and p-type operation. Recently, one-step annealed (600 °C at a O_2 partial pressure of 2×10^{-6} Torr,) CuO_x TFTs were also demonstrated[59], yielding p-type TFTs with $\mu_h \approx$ 0.29 cm^2 V^{-1} s^{-1}. The paucity of p-type MOs suggests a challenging research opportunity.

Spray pyrolysis. Pioneering ZnO studies revealed the potential and versatility of this technique for high-performance MO devices. ZnO TFTs were fabricated at temperatures as low as 200 °C by spray coating aqueous zinc acetate or methanol solutions, achieving μ_e ~0.1 cm^2 V^{-1} s^{-1}, which increases to ~15 cm^2 V^{-1} s^{-1} with 400 °C processing[60]. Furthermore, low-voltage ZnO TFT operation was achieved by integrating spray-coated ZnO films with high-k gate dielectrics, and a low-voltage (<2 V) unipolar MO inverter was fabricated with two TFTs. Other n-type compositions and conditions were recently explored (Table 2). The only spray-coated p-type TFTs were fabricated by spraying aqueous $Cu(OAc)_2$ solutions on Si–SiO_2 substrates at 275 °C (ref. 61). These CuO_x TFTs exhibit $\mu_h \approx 10^{-4}$–10^{-3} cm^2 V^{-1} s^{-1}.

© 2016 Macmillan Publishers Limited. All rights reserved

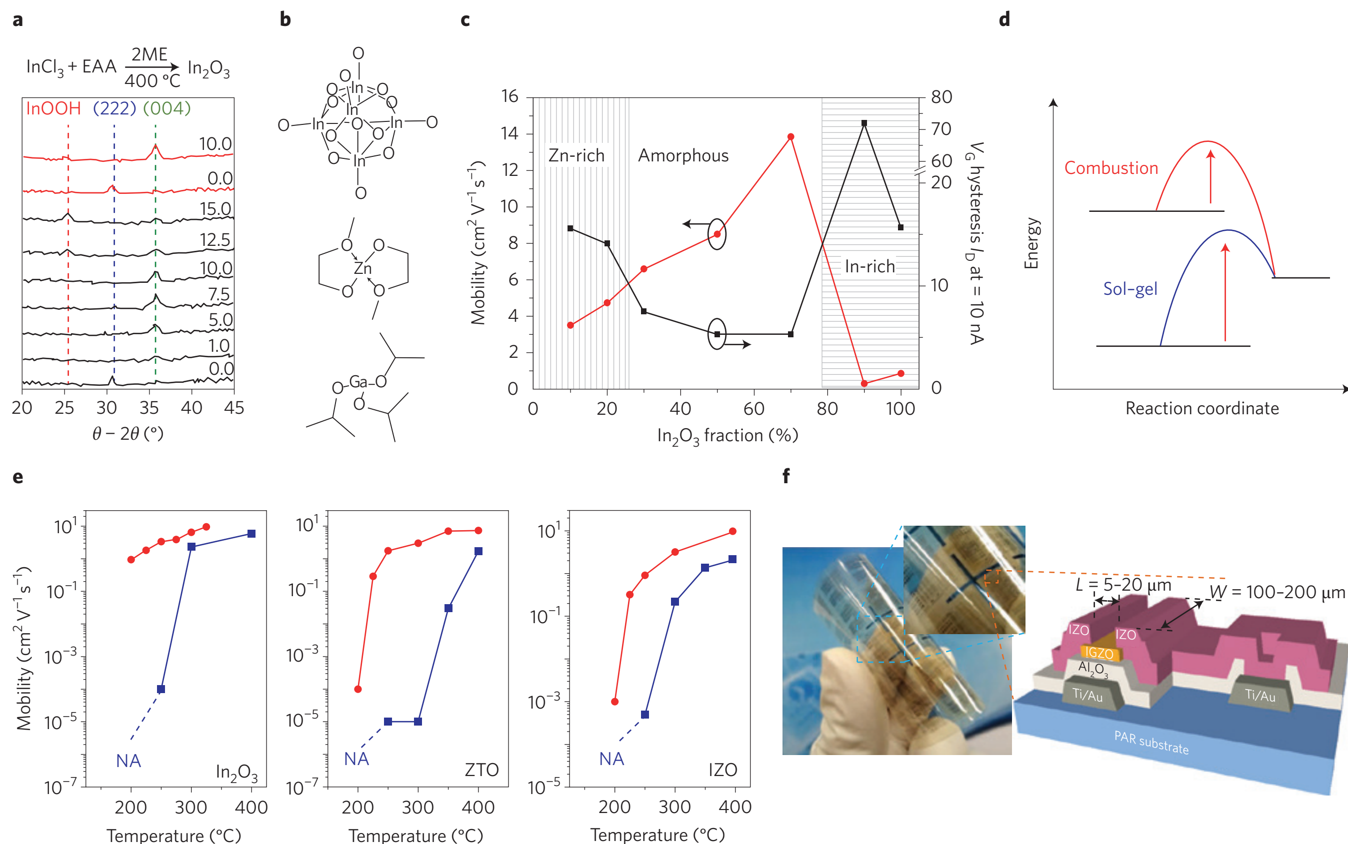

Figure 3 | Solution-processed metal oxide. a, X-ray diffraction-derived microstructure evolution for various In_2O_3 films fabricated with different In:ethanolamine (EAA) molar ratios (indicated as mol%). Black scans are Si-SiO_2 substrates; red scans are Si-self-assembled nano-dielectric substrates. ME, methoxyethanol. **b**, Metal oxide precursors used in the 'sol-gel on a chip' process: indium alkoxide cluster, zinc-bis-methoxyethoxide and gallium-tris-isopropoxide. **c**, Mobility and gate voltage (V_G) hysteresis variations versus In_2O_3 atomic fraction in IZO TFTs. **d**, Energetics of combustion synthesis-based film growth versus the conventional sol-gel process (top) and the combustion synthetic chemistry (bottom); the red arrows define the input energy required for M-O-M formation. **e**, Mobility versus annealing temperature for the indicated metal oxide-based TFTs (In_2O_3, ZTO and IZO) using combustion (red) and sol-gel (blue) synthesis. NA, data not available. **f**, Optical images and a schematic cross-section of photo-annealed IGZO TFTs and circuits on polyarylate (PAR) substrates. *L*, channel length; *W*, channel width. Figures reproduced from: **a**, ref. 43, American Chemical Society; **b**,**c**, ref. 47, NPG; **d**,**e**, ref. 62, NPG; **f**, ref. 49, NPG.

Combustion synthesis. An alternative route to lowering solution-deposited MO film processing temperatures is combustion synthesis, where fuel and oxidizer pairs imbue MO precursor solutions with large internal energies. This creates self-generated exotherms within MO films versus conventional, highly endothermic sol–gel condensations. After precursor deposition and minimal heating to initiate combustion, the self-generated, localized heat drives M-O-M lattice formation and densification (Fig. 3d).

The first combustion experiments demonstrated In_2O_3, a-IZO, and a-ZTO films fabricated at temperatures as low as 200 °C (ref. 62), with redox-based urea or acetylacetone fuel and $M(NO_3)_x$ as chemical precursor fuel–oxidizer pairs. For TFT fabrication, such combined solutions were spin-coated on doped-Si–SiO_2 substrates, the resulting films annealed at 200–400 °C and the process repeated until ~20–30 nm MO films were achieved; finally, Al source–drain contacts were deposited on top. The advantage of combustion synthesis is evident by comparing sol–gel-derived and combustion synthesis MO TFT performance. In fact, processing In_2O_3 films by combustion at 200 °C yielded TFTs with $\mu_e \approx 1$ cm^2 V^{-1} s^{-1} (on Si–SiO_2), whereas sol–gel TFTs are inactive (Fig. 3e). Similar trends hold for the other MO semiconductors, with results understandable in terms of improved film morphology and composition evolution with annealing temperature. Furthermore, In_2O_3 TFT μ_e increases to ~40 cm^2 V^{-1} s^{-1} for an annealing temperature of 250 °C using a higher-*k* gate insulator. This approach was subsequently expanded to other semiconductors, including indium yttrium oxide (IYO), IGO, ZnO, IGZO, indium yttrium zinc oxide (IYZO), and indium lanthanum zinc oxide (ILZO)[63–65]. Here a-IXZO (In–X–Zn–O, X = Ga, Sc, Y, La) compositions clarified how metal X stabilizes amorphous phases and/or acts as an O 'getter' to optimize carrier concentrations and bias-stress stability. MO combustion synthesis has now been reported by several groups (Table 2), demonstrating its generality. To better understand amorphous phase transport in such films, combustion-derived InXO materials were prepared for X = Sc, Y, and La. The results show that cations with radii larger than In(III) induce amorphous character and achieve high μ_e at very low X concentrations (~5% for La). Furthermore, increased ionic radii correlate with broader tail-state trap distributions in the trap-limited conduction regime, and with greater potential barrier heights in the percolation regime. These results agree well with local structure information determined from *ab initio* molecular dynamics simulations[66]. Interestingly, by combining combustion-processed IGZO with a sorted p-type CNT network, antiambipolar heterojunction circuits based on two TFTs and one resistor have been recently demonstrated[67], whereas in conventional Si-integrated communications at least seven TFTs are required to create such circuits.

Recently, a versatile new growth process combining spray coating with combustion synthesis (SCS, spray combustion synthesis) was reported[68]. The combined internal combustion heat and spray-suppressed gaseous by-product trapping during film growth yields

© 2016 Macmillan Publishers Limited. All rights reserved

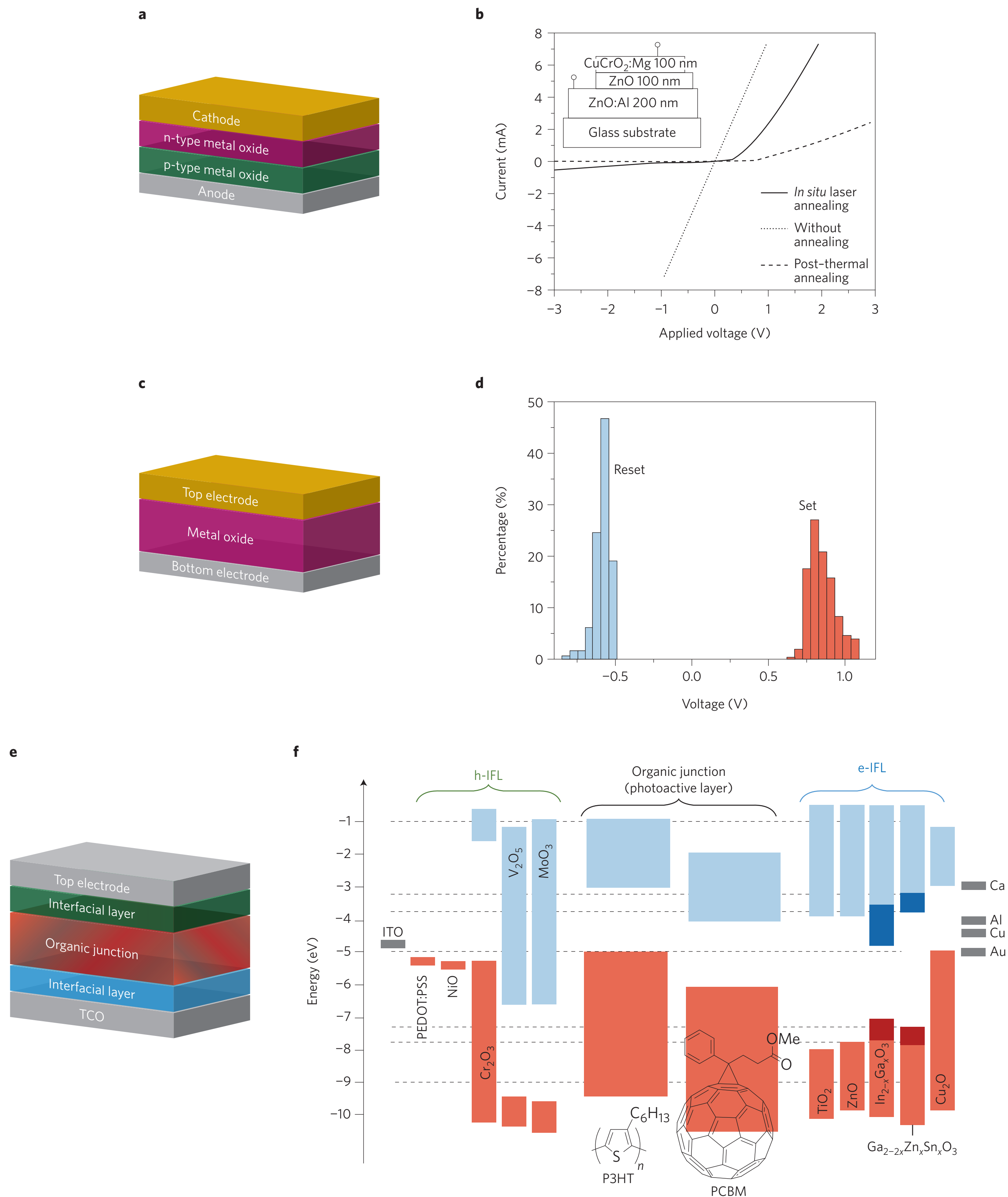

Figure 4 | Metal oxide electronics. a, Schematic of a p–n junction device. **b**, Current–voltage characteristics of a ZnO(n)–ZnO:Al(p) diode (inset) processed under the indicated conditions. **c**, Random access memory schematic. **d**, Distribution of the set and reset voltages for d.c. sweep in a TiN–ZrO_2–Pt memory cell stack. **e**, Schematic of an organic solar cell. TCO, transparent conducting oxide. **f**, Energy-level schematic depiction for selected organic solar cell materials and metal oxide electron and hole interfacial layers (e-IFLs and h-IFLs). The grey, light blue and red colours represent work functions, lowest unoccupied molecular orbital (LUMO) levels and highest occupied molecular orbital (HOMO) levels, respectively. The dark blue and dark red regions indicate the energy range for LUMO and HOMO levels, respectively, which depends on the metal oxide composition. Dashed lines are guides for the eyes. Figures reproduced from: **b**, ref. 80, Elsevier; **d**, ref. 93, AIP.

© 2016 Macmillan Publishers Limited. All rights reserved

ultra-high-quality, dense (by positron annihilation spectroscopy and X-ray reflectivity) In_2O_3, IZO and IGZO films in remarkably short growth times. SCS produces ~50 nm a-IGZO films (minimal thickness for commercial applications) in ~30 min, with TFT performance far superior to spin-coated combustion films (requiring ≥4 h growth times) and with comparable mobility, defect densities and V_T shift (~1 V) to sputtered films.

Pre-formed nanostructures for transistors

Besides films, MO nanomaterials have been used in TFT channels. Oxide nanostructures show large carrier mobilities, yet controlling the density and orientation of these nanostructures on a large scale is challenging. The most successful TFTs employ ZnO, SnO_2 nanocrystals, and In_2O_3 nanowires and nanoribbons[69–71]. TFTs based on transparent In_2O_3 and ZnO nanowires spin-coated on PET have $\mu_e > 500$ cm^2 V^{-1} s^{-1} and ~100 cm^2 V^{-1} s^{-1} ($I_{on/off} \approx 10^6$), respectively[72]. Remarkably, p-type CuO_x nanowires thermally grown on Cu foil at 500 °C and then transferred to Si–SiO_2 substrates[73], yield TFTs with $\mu_h \approx 15$ cm^2 V^{-1} s^{-1}. Advances have also been made in moving from single-wire devices to nanomaterial networks. For instance, ZnO nanorod TFTs with $\mu_e \approx 0.6$ cm^2 V^{-1} s^{-1} were fabricated by hydrothermal growth, immersing spin-coated ZnO nanorod films in aqueous $Zn(NO_3)_2$ at 90 °C (ref. 74). Similarly, a ZnO nanowire network was fabricated with spin-coated ZnO quantum dots as seeds, followed by immersion in aqueous $Zn(NO_3)_2$ for nanowire network growth at <140 °C (ref. 75). The resulting TFTs exhibit $\mu_e = 0.2$ cm^2 V^{-1} s^{-1}, but suffer from grain boundary effects. Spin-coated ZnO nanoparticles treated with $Zn(NO_3)_2$ solutions afford higher μ_e, ~1.75 cm^2 V^{-1} s^{-1} (ref. 76).

p–n junction devices

Diodes can be fabricated by combining p- and n-type MO layers to form p–n junctions (Fig. 4a). A conducting anode, a semiconductor p–n junction and a conducting cathode achieve rectifying current–voltage characteristics, for applications such as diode rectifiers, sensors and solar cells. However, MO p–n junctions are rare due to the limited selection of p-type MO semiconductors. The demonstration of p-type $CuAlO_2$ films by PLD growth[77], followed by p-type $CuGaO_2$ (ref. 14) and $SrCu_2O_2$ (ref. 78) film growth, led to the first MO p–n junction diode in 2000. Such a device was composed of a sputtered $SrCu_2O$–n$^+$ZnO bilayer and ITO electrodes, and exhibited a rectification ratio of ~80 from −1.5 to 1.5 V (ref. 79). In 2008, a p–n junction diode was fabricated with Mg-doped $CuCrO_2$ (p-type) and ZnO (n-type) films, using PLD-grown AZO electrodes fabricated at room temperature (Fig. 4b). A rectification ratio of ~50 from −2 to 2 V was reported[80].

MO diodes for gas sensors using various p–n junction architectures have been investigated, including semiconductor blends[81,82], and core–shell[83,84], bilayer or multilayer structures[85,86]. However, such sensors typically require >200 °C operating temperatures to reach the molecular adsorption and desorption rates required for high responsivity. Recently, resonant tunnelling devices using Cu_2O–SnO_2 p–n multilayer heterostructures were reported to exhibit excellent sensitivity to H_2S vapours at 25 °C (ref. 87). Some studies have also proposed all-MO diodes for photovoltaic cells. Here, Al-doped ZnO(n-type)–Ga_2O_3(i)–Cu_2O(p-type) thin-film heterojunction solar cells fabricated at 25 °C by PLD gave power conversion efficiencies (PCEs) of 5.38%, higher than optimized Cu_2O solar cells[88]. Recently, nanosized ZnO(n)–Cu_2O(p) and ZnO(n)–TiO_2(i)–Cu_2O(p) heterostructure diodes were fabricated from vapour-phase-synthesized Cu_2O nanowires[89], and a PCE of 0.39% was measured, suggesting the possibility of practical nanostructured oxide heterojunction solar cells.

Memories

Random access memories (RAMs) are important data-storage components in logic circuits, and MOs are well-suited for resistive RAMs (ReRAMs) and floating-gate TFT flash memories (Fig. 4c). So far, several MOs have been employed in ReRAMs, with an oxide layer sandwiched between two electrodes. Key performance metrics are the programming set and reset voltages V_{set} and V_{reset}, respectively, and the low-resistance state/high-resistance state ratio[90]. In 2008, a ReRAM with an Al electrode on top of CuO_x–Cu (MO–bottom electrode) was demonstrated, exhibiting programming voltages $V_{set} = 3$ V, $V_{reset} = -1$ V, and a resistance ratio $>10^3$ (ref. 91). ReRAM switching speeds also depend on the memory element size, so scaling down device sizes can increase performance. In another study, 100 nm × 100 nm ReRAMs were fabricated with ALD-grown NiO as the MO and Pt electrodes, and exhibited $V_{set} \approx 1.5$ V, $V_{reset} \approx 0.6$ V, and a resistance ratio of ~10^2 (ref. 92). ReRAMs using sol–gel ZrO_2 annealed at 600 °C, exhibit $V_{set} \approx 0.8$ V, $V_{reset} \approx -0.5$ V, and a resistance ratio of >10 (Fig. 4d)[93]. Also, nonvolatile resistance switching was achieved using sputtered ZnO with ITO electrodes on plastic (polyethersulfone) substrates, demonstrating transparent flexible ReRAMs with $V_{set} \approx 1.5$ V, $V_{reset} \approx 0.5$ V, and a resistance ratio of ~10^2 (ref. 94).

Flash memories are the most common memory configuration due to their excellent compatibility with the CMOS circuitry used to address each memory cell, and show reliable and uniform memory characteristics, fast switching and non-destructive readout. In the most common flash memories, charge storage relies on trapped charge carriers in a floating gate within the SiO_2 or SiN_x gate dielectric, or in a non-conductive discrete trapping layer. MO materials are suitable for memory devices as non-conducting trapping layers in the dielectric or in the TFT channel[95]. In 1995, a MO memory TFT was created with PLD-grown perovskite semiconducting ($La_{1.99}Sr_{0.01}CuO_4$) and dielectric ((Pb,La)(Zr,Ti)O_3) layers. These devices can be written and erased at 7 V with a pulse width of less than 1 ms (ref. 96). Recently, solution-processed TFT-based memories were fabricated with spin-coated MO semiconductor channels (In_2O_3, IGO) and a solution-processed Cu-doped zirconia (Cu–ZrO_x) composite acting as an electrochemical redox trapping layer within the gate dielectric[97]. Using a high-capacitance self-assembled nanodielectric layer, these TFT memories demonstrated $\mu_e \approx 2.5$ cm^2 V^{-1} s^{-1}, good reliability and operation below 3 V.

Organic solar cells

Organic photovoltaic (OPV) cells are excitonic devices, converting light into electricity, where the p–n junction photoactive layer is composed of organic semiconductors. The most investigated OPV architecture has a bottom TCO electrode, a bulk-heterojunction blend of donor (p-type) and acceptor (n-type) organic semiconductors, charge extracting layers and a top metal electrode (Fig. 4e). Depending on the semiconductor/electrode interface arrangement, the transparent electrode collects holes and the metal electrode electrons ('conventional' architecture) or vice versa ('inverted' architecture). MOs are typically employed as the TCO electrode or as charge-extracting interfacial layers (IFLs) to enhance PCE. The electron concentration (N) and carrier mobility affect TCO electrical and optical properties, with N affecting both the short wavelength transmittance cut-off limit (band gap) and the long wavelength transmittance cut-off (plasma wavelength)[98]. Typically, these optical limitations shift to shorter wavelengths with increasing N, and for solar applications, high carrier mobility and low-N TCOs are preferred. As an exception to this rule, electronic structure engineering rather than doping has been recently used to suppress interband transitions in thermal epitaxy-grown $SrVO_3$ and $CaVO_3$ films, yielding high conductivity and transparency[99] even in the presence of high carrier concentrations ($N > 2.2 \times 10^{22}$ cm^{-3}). Strong electron–electron interactions in these correlated materials lead to low screened plasma energies (<1.33 eV) and good combined conductivity and transparency performance.

© 2016 Macmillan Publishers Limited. All rights reserved

Wide bandgap MOs, for example, In_2O_3, SnO_2 and ZnO, are useful TCOs by keeping $N < 10^{18}$ cm^{-3} and adding secondary dopant ions to increase the optical bandgap (Burstein-Moss effect). Thus, the bandgaps of InAlO (ref. 100) and ZnGaO (ref. 101) (~3.8 eV) are higher than the parent In_2O_3 (~3.7 eV) or ZnO (~3.2 eV) host. However, ITO is by far the most used TCO electrode for organic solar cells (OSCs) considering the low sheet resistance (~10 Ω sq.$^{-1}$), excellent transparency (optical bandgap ~4.0 eV), minimal toxicity, good etchability and facile film formation on glass and plastic substrates[12]. Good ITO conductivity minimizes resistive losses to the collecting electrodes, whereas the transparency increases light absorption in the photoactive layer. Resistive losses become significant in OSCs, especially for large-area devices (>0.1 cm^2), and simulations reveal that hole-collecting electrode conductivity contributes significantly to these losses[102]. It has been shown that OSC PCEs increase from 5.94 to 8.24%, when the hole-collecting ITO sheet resistance decreases from 40 to 5 Ω sq.$^{-1}$ (ref. 103). Other TCOs have been utilized in OSCs such as zinc indium tin oxide (ZITO; ~10 Ω sq.$^{-1}$)[104] and $In_xCd_{1-x}O$–ITO bilayers (~5.5 Ω sq.$^{-1}$)[105]. Usually, polycrystalline TCO films on plastic suffer from significant performance degradation and cracking on tension and compressive mechanical stress. However, it was recently shown that PLD-grown a-ZITO on AryLite plastic is an excellent OPV electrode, with a sheet resistance of ~20 Ω sq.$^{-1}$ and superior mechanical stability on multiple bends about a 5 mm radius[106]. Flexible AryLite–a-ZITO-based PTB7:PC71BM cells provide PCE = 6.42%.

MO films have also been extensively used as IFLs for hole (h-IFL) or electron (e-IFL) selective extraction from OSC active layers, both in conventional and inverted device architectures (Fig. 4f). In conventional architectures, MO h-IFLs are primarily used to replace the corrosive hole conductor PEDOT:PSS on ITO. In 2008, the first use of PLD-grown NiO as a p-type h-IFL in P3HT:PCBM cells was reported, yielding an optimized PCE of 5.16% for a 10-nm-thick NiO IFL versus 2.87% for the control[107]. In 2010, solution-processed NiO was deposited by spin-coating a Ni-based ink on ITO and annealing at 250 °C, affording P3HT:PCBM cells with PCE = 3.6% — comparable to PEDOT:PSS cells[108]. Recently, PLD-grown NiO films were studied as a function of processing parameters, such as atmospheric gas ratio and growth temperature as well as post-deposition Ar and O_2 plasma treatment, to assess effects on film electronic structure and OPV performance[109]. Interestingly, substantial NiO work-function changes of ~1 eV occur on O_2 plasma treatment. Other MOs commonly used to replace PEDOT:PSS as an h-IFL are vapour-deposited V_2O_5 (ref. 110), MoO_3 and WO_3 (refs 111,112). The Fermi levels of these materials are very near the CBM and technically are n-type semiconductors[113], yet they may function as p-type dopants for the photoactive blend donor material (for instance P3HT) considering that their CBM lies below the donor highest occupied molecular orbital energy[114]. MoO_3 films prepared by spin-coating nanoparticle suspensions exhibit properties similar to vapour-deposited films[115,116]. Sol–gel deposited V_2O_5 films spin-coated and then annealed at low temperatures[110] yield OSCs with performance comparable to PEDOT:PSS cells but with improved durability.

The most common electron-extracting MO e-IFLs in conventional OSC architectures typically replace LiF in contact with the electron-collecting electrode, and are n-type TiO_2 and ZnO. Furthermore, amorphous TiO_2 films have been fabricated by spin-coating sol–gels directly on the OSC photoactive layer at temperatures compatible with the organic materials[117]. ZnO has a higher μ_e than TiO_2, mitigating recombination losses. Although sol–gels have been used for ZnO IFLs, spin-coatable nanoparticle formulations are more broadly used[118].

For inverted OSC architectures, MOs can be used to switch the ITO function from hole- to electron-collecting, thereby extracting electrons and accommodating high work-function and stable top-electrode metals. Typical inverted OPVs use sol–gel-derived ZnO e-IFLs on the ITO electrode[119–122], however, Cs_2CO_3 (ref. 123) and TiO_2 (ref. 124) have also been reported. Again, nanoparticle-based formulations allow process simplification, effectively eliminating high-temperature sol–gel annealing and enhancing the device lifetime[125]. Triple-junction OCSs with multiple photoactive layers have been recently fabricated using Li-doped ZnO interlayers (spin-coated, annealed at 100 °C), to achieve a PCE = 11.83% (ref. 126). Furthermore, ITO–ZnO electrodes have been combined with various MO h-IFLs, such as thermally evaporated V_2O_5 and MoO_3, and various organic active materials[127]. Besides sol–gel methods, ALD was used to grow interfacial MO layers for OSCs at low temperatures[128]. Using ALD-grown ZnO as an e-IFL (36 nm, at 80 °C) yields P3HT:PCBM cells with PCE = 4.18% on flexible PET substrates[129]. Thermally evaporated PbO has also been used as an e-IFL for inverted devices, lowering the ITO work function by ~1 eV (ref. 130). PbO-based P3HT:PCBM cells in combination with a MoO_3 h-IFL at the metal hole-collecting electrode give PCEs of ~4.00%. Regarding h-IFLs, amorphous V_2O_5 solutions processed at ~100 °C (ref. 131) and CuO_x sol–gels have also been used in inverted P3HT:PCBM cells[132]. Similar to p-type NiO, CuO_x has a CBM at ~5.3 eV, matching the P3HT highest occupied molecular orbital for hole extraction. Such cells have a PCE of ~4.02% with stability >1,000 h.

It should be mentioned that metal nanowire meshes — typically silver nanowire (AgNW) networks — have emerged as promising electrodes for OSCs. However, due to the large injection barrier between AgNWs and organic semiconductors, the OSCs suffer low performance. Therefore, MO h-IFLs and/or e-IFLs are also used to replace PEDOT:PSS and/or LiF, respectively. Inverted P3HT:PCBM cells with a AgNW-based electron-collecting electrode utilized spin-coated TiO_x and evaporated MoO_x as the e-IFL and h-IFL, respectively, affording a PCE of 3.1% versus 2.0% for PEDOT:PSS h-IFL devices[133]. Recently, fully printed tandem OSCs on PET plastic substrates using AgNW-based electron-collecting electrodes and ZnO e-IFLs achieved an optimized PCE of 4.85% (ref. 134). These results demonstrate the potential of combining these two types of materials to engineer transparent electrodes.

Outlook

Great progress has been made in understanding and implementing new metal oxide optoelectronic materials, including crystalline and amorphous transparent conductors (TCOs) and semiconductors. These materials now rival and complement other unconventional semiconductors such as organics, CNTs and 2D materials. Capitalizing on unique MO properties, numerous electronic and optical devices have been demonstrated, with many notable advances in the past several years. These include the following: (i) Advances in p-type semiconductors, opening possibilities for p-type TFTs, p–n junctions and oxide CMOS. Considering that, in contrast to organics and CNTs, MO transport has been largely limited to electrons, this advance significantly changes our understanding of how MOs can be tuned for new functions. Nevertheless, additional fundamental studies are needed to bridge the performance gap between n- and p-type MO semiconductors. (ii) The demonstration of unique charge-transport properties of AOSs versus a-Si:H and a-chalcogenides, which enable performance not possible in a-chalcogenide materials. (iii) Low-temperature film growth on diverse substrates, including plastics, by a variety of techniques. This has enabled the realization of high performance, flexible, and transparent TFTs, with IGZO currently commercialized for OLED and next-generation liquid-crystal display backplane drivers. An interesting question is whether less complex MOs can achieve IGZO performance and stability, with broader process windows. (iv) Advances in solution-based MO deposition via numerous new techniques, including those using MO nanoparticles and nanowires. Various direct solution-phase MO film growth techniques

© 2016 Macmillan Publishers Limited. All rights reserved

have been developed, including sol–gel, spray pyrolysis, chemical bath deposition, direct oxidation of solution-deposited precursors and combustion synthesis. In optimum cases, the performance approaches that achieved by capital-intensive vapour-phase growth technologies. Although MO processing temperatures for optimal performance remain higher than those of the best organic semiconductor devices, the gap between performance and processing temperature is falling. Given the excellent stability and transparency of a-MOs, it is likely that further understanding-based optimization will yield performance more comparable to gas-phase growth; this, together with the excellent stability and transparency of AOS, will lead to the realization of high-performance, large-area electronics on a wide range of substrates.

Received 25 August 2015; accepted 15 February 2016; published online 23 March 2016

References

1. Spear, W. & Le Comber, P. Substitutional doping of amorphous silicon. *Solid State Commun.* **17,** 1193–1196 (1975).
2. Klasens, H. A. & Koelmans, H. A tin oxide field-effect transistor. *Solid State Electron.* **7,** 701–702 (1964).
3. Nomura, K. *et al.* Thin-film transistor fabricated in single-crystalline transparent oxide semiconductor. *Science* **300,** 1269–1272 (2003).
4. Wang, L. *et al.* High-performance transparent inorganic–organic hybrid thin-film n-type transistors. *Nature Mater.* **5,** 893–900 (2006).
5. Presley, R. *et al.* Tin oxide transparent thin-film transistors. *J. Phys. D: Appl. Phys.* **37,** 2810–2813 (2004).
6. Hoffman, R., Norris, B. J. & Wager, J. ZnO-based transparent thin-film transistors. *Appl. Phys. Lett.* **82,** 733–735 (2003).
7. Denton, E. P., Rawson, H. & Stanworth, J. E. Vanadate Glasses. *Nature* **173,** 1030–1032 (1954).
8. Nomura, K. *et al.* Room-temperature fabrication of transparent flexible thin-film transistors using amorphous oxide semiconductors. *Nature* **432,** 488–492 (2004).
9. Kamiya, T., Nomura, K. & Hosono, H. Origins of high mobility and low operation voltage of amorphous oxide TFTs: electronic structure, electron transport, defects and doping. *J. Disp. Technol.* **5,** 273–288 (2009).
10. Kimura, M. *et al.* Extraction of trap densities in ZnO thin-film transistors and dependence on oxygen partial pressure during sputtering of ZnO films. *IEEE Trans. Electron. Dev.* **58,** 3018–3024 (2011).
11. Hsieh, H.-H., Kamiya, T., Nomura, K., Hosono, H. & Wu, C.-C. Modeling of amorphous $InGaZnO_4$ thin film transistors and their subgap density of states. *Appl. Phys. Lett.* **92,** 133503 (2008).
12. Facchetti, A. & Marks, T. J. *Transparent Electronics: From Synthesis to Application* (Wiley, 2010).
13. Fortunato, E., Barquinha, P. & Martins, R. Oxide semiconductor thin-film transistors: a review of recent advances. *Adv. Mater.* **24,** 2945–86 (2012).
14. Yanagi, H., Kawazoe, H., Kudo, A., Yasukawa, M. & Hosono, H. Chemical design and thin film preparation of p-type conductive transparent oxides. *J. Electroceram.* **4,** 407–414 (2000).
15. Forrest, S. R. The path to ubiquitous and low-cost organic electronic appliances on plastic. *Nature* **428,** 911–918 (2004).
16. Anthony, J. E. Organic electronics: addressing challenges. *Nature Mater.* **13,** 773–775 (2014).
17. Cao, Q. *et al.* Medium-scale carbon nanotube thin-film integrated circuits on flexible plastic substrates. *Nature* **454,** 495–500 (2008).
18. Li, Z., Liu, Z., Sun, H. & Gao, C. Superstructured assembly of nanocarbons: fullerenes, nanotubes, and graphene. *Chem. Rev.* **115,** 7046–7117 (2015).
19. Schmidt, H., Giustiniano, F. & Eda, G. Electronic transport properties of transition metal dichalcogenide field-effect devices: surface and interface effects. *Chem. Soc. Rev.* **44,** 7715–7736 (2015).
20. Aoki, A. & Sasakura, H. Tin oxide thin film transistors. *Jpn J. Appl. Phys.* **9,** 582 (1970).
21. Carcia, P. F., McLean, R. S., Reilly, M. H. & Nunes, G. Transparent ZnO thin-film transistor fabricated by RF magnetron sputtering. *Appl. Phys. Lett.* **82,** 1117 (2003).
22. Brox-Nilsen, C., Jidong, J., Yi, L., Peng, B. & Song, A. M. Sputtered ZnO thin-film transistors with carrier mobility over 50 $cm^2 V^{-1} s^{-1}$. *IEEE Trans. Electron. Dev.* **60,** 3424–3429 (2013).
23. Lee, E. *et al.* Gate capacitance-dependent field-effect mobility in solution-processed oxide semiconductor thin-film transistors. *Adv. Funct. Mater.* **24,** 4689–4697 (2014).
24. Lin, Y.-Y., Hsu, C.-C., Tseng, M.-H., Shyue, J.-J. & Tsai, F.-Y. Stable and high-performance flexible ZnO thin-film transistors by atomic layer deposition. *ACS Appl. Mater. Interfaces* **7,** 22610–22617 (2015).
25. Se Yeob, P. *et al.* Improvement in photo-bias stability of high-mobility indium zinc oxide thin-film transistors by oxygen high-pressure annealing. *IEEE Electr. Dev. Lett.* **34,** 894–896 (2013).
26. Joo Hyon, N. *et al.* Indium oxide thin-film transistors fabricated by RF sputtering at room temperature. *IEEE Electr. Dev. Lett.* **31,** 567–569 (2010).
27. Yabuta, H. *et al.* High-mobility thin-film transistor with amorphous $InGaZnO_4$ channel fabricated by room temperature RF-magnetron sputtering. *Appl. Phys. Lett.* **89,** 112123 (2006).
28. Chowdhury, M. D. H., Migliorato, P. & Jang, J. Time-temperature dependence of positive gate bias stress and recovery in amorphous indium-gallium-zinc-oxide thin-film-transistors. *Appl. Phys. Lett.* **98,** 153511 (2011).
29. Jung, J. S. *et al.* The impact of SiN_x gate insulators on amorphous indium-gallium-zinc oxide thin film transistors under bias-temperature-illumination stress. *Appl. Phys. Lett.* **96,** 193506 (2010).
30. Moon, Y.-K. *et al.* Improvement in the bias stability of amorphous indium gallium zinc oxide thin-film transistors using an O_2 plasma-treated insulator. *Appl. Phys. Lett.* **95,** 013507 (2009).
31. Nomura, K., Kamiya, T., Hirano, M. & Hosono, H. Origins of threshold voltage shifts in room-temperature deposited and annealed a-In-Ga-Zn-O thin-film transistors. *Appl. Phys. Lett.* **95,** 013502 (2009).
32. Kim, M.-M., Kim, M.-H., Ryu, S.-m., Lim, J. & Choi, D.-K. Coplanar homojunction a-InGaZnO thin film transistor fabricated using ultraviolet irradiation. *RSC Adv.* **5,** 82947–82951 (2015).
33. Barquinha, P., Pereira, L., Goncalves, G., Martins, R. & Fortunato, E. Toward high-performance amorphous GIZO TFTs. *J. Electrochem. Soc.* **156,** H161–H168 (2009).
34. Ogo, Y. *et al.* P-channel thin-film transistor using p-type oxide semiconductor, SnO. *Appl. Phys. Lett.* **93,** 032113 (2008).
35. Martins, R. F. P. *et al.* Recyclable, flexible, low-power oxide electronics. *Adv. Funct. Mater.* **23,** 2153–2161 (2013).
36. Matsuzaki, K. *et al.* Epitaxial growth of high mobility Cu_2O thin films and application to p-channel thin film transistor. *Appl. Phys. Lett.* **93,** 202107 (2008).
37. Fortunato, E. *et al.* Thin-film transistors based on p-type Cu_2O thin films produced at room temperature. *Appl. Phys. Lett.* **96,** 192102 (2010).
38. Sanal, K. C., Vikas, L. S. & Jayaraj, M. K. Room temperature deposited transparent p-channel CuO thin film transistors. *Appl. Surf. Sci.* **297,** 153–157 (2014).
39. Jeong, S. & Moon, J. Low-temperature, solution-processed metal oxide thin film transistors. *J. Mater. Chem.* **22,** 1243–1250 (2012).
40. Ohya, Y., Niwa, T., Ban, T. & Takahashi, Y. Thin film transistor of ZnO fabricated by chemical solution deposition. *Jpn J. Appl. Phys.* **40,** 291–298 (2001).
41. Ong, B. S., Li, C., Li, Y., Wu, Y. & Loutfy, R. Stable, solution-processed, high-mobility ZnO thin-film transistors. *J. Am. Chem. Soc.* **129,** 2750–2751 (2007).
42. Lin, Y.-H. *et al.* High-performance ZnO transistors processed via an aqueous carbon-free metal oxide precursor route at temperatures between 80–180 °C. *Adv. Mater.* **25,** 4340–4346 (2013).
43. Kim, H. S., Byrne, P. D., Facchetti, A. & Marks, T. J. High performance solution-processed indium oxide thin-film transistors. *J. Am. Chem. Soc.* **130,** 12580–12581 (2008).
44. Han, S.-Y., Herman, G. S. & Chang, C.-h. Low-temperature, high-performance, solution-processed indium oxide thin-film transistors. *J. Am. Chem. Soc.* **133,** 5166–5169 (2011).
45. Rim, Y. S. *et al.* Simultaneous modification of pyrolysis and densification for low-temperature solution-processed flexible oxide thin-film transistors. *J. Mater. Chem.* **22,** 12491–12497 (2012).
46. Hwan Hwang, Y. *et al.* An 'aqueous route' for the fabrication of low-temperature-processable oxide flexible transparent thin-film transistors on plastic substrates. *NPG Asia Mater.* **5,** e45 (2013).
47. Banger, K. K. *et al.* Low-temperature, high-performance solution-processed metal oxide thin-film transistors formed by a 'sol-gel on chip' process. *Nature Mater.* **10,** 45–50 (2011).
48. Jeong, S. *et al.* Metal salt-derived In-Ga-Zn-O semiconductors incorporating formamide as a novel co-solvent for producing solution-processed, electrohydrodynamic-jet printed, high performance oxide transistors. *J. Mater. Chem. C* **1,** 4236–4243 (2013).
49. Kim, Y. H. *et al.* Flexible metal-oxide devices made by room-temperature photochemical activation of sol-gel films. *Nature* **489,** 128–132 (2012).
50. Lin, Y.-H. *et al.* High electron mobility thin-film transistors based on solution-processed semiconducting metal oxide heterojunctions and quasi-superlattices. *Adv. Sci.* **2,** 1500058 (2015).
51. Perelaer, J. *et al.* Printed electronics: the challenges involved in printing devices, interconnects, and contacts based on inorganic materials. *J. Mater. Chem.* **20,** 8446–8453 (2010).

© 2016 Macmillan Publishers Limited. All rights reserved

52. Choi, C.-H., Lin, L.-Y., Cheng, C.-C. & Chang, C.-h. Printed oxide thin film transistors: a mini review. *ECS J. Solid State Sci. Technol.* **4,** P3044–P3051 (2015).
53. Lee, D. H., Chang, Y. J., Herman, G. S. & Chang, C. H. A general route to printable high-mobility transparent amorphous oxide semiconductors. *Adv. Mater.* **19,** 843–847 (2007).
54. Lee, W. H., Lee, S. J., Lim, J. A. & Cho, J. H. Printed In-Ga-Zn-O drop-based thin-film transistors sintered using intensely pulsed white light. *RSC Adv.* **5,** 78655–78659 (2015).
55. Choi, Y. *et al.* Characteristics of gravure printed InGaZnO thin films as an active channel layer in thin film transistors. *Thin Solid Films* **518,** 6249–6252 (2010).
56. Leppäniemi, J., Huttunen, O.-H., Majumdar, H. & Alastalo, A. Flexography-printed In_2O_3 Semiconductor layers for high-mobility thin-film transistors on flexible plastic substrate. *Adv. Mater.* **27,** 7168–7175 (2015).
57. Spiehl, D., Haming, M., Sauer, H. M., Bonrad, K. & Dorsam, E. Engineering of flexo- and gravure-printed indium–zinc-oxide semiconductor layers for high-performance thin-film transistors. *IEEE Trans. Electr. Dev.* **62,** 2871–2877 (2015).
58. Hong, K., Kim, S. H., Lee, K. H. & Frisbie, C. D. Printed, sub-2V ZnO electrolyte gated transistors and inverters on plastic. *Adv. Mater.* **25,** 3413–3418 (2013).
59. Yu, J. *et al.* Solution-processed p-type copper oxide thin-film transistors fabricated by using a one-step vacuum annealing technique. *J. Mater. Chem. C* **3,** 9509–9513 (2015).
60. Bashir, A. *et al.* High-performance zinc oxide transistors and circuits fabricated by spray pyrolysis in ambient atmosphere. *Adv. Mater.* **21,** 2226–2231 (2009).
61. Pattanasattayavong, P., Thomas, S., Adamopoulos, G., McLachlan, M. A. & Anthopoulos, T. D. P-channel thin-film transistors based on spray-coated Cu_2O films. *Appl. Phys. Lett.* **102,** 163505 (2013).
62. Kim, M. G., Kanatzidis, M. G., Facchetti, A. & Marks, T. J. Low-temperature fabrication of high-performance metal oxide thin-film electronics via combustion processing. *Nature Mater.* **10,** 382–388 (2011).
63. Hennek, J. W., Kim, M.-G., Kanatzidis, M. G., Facchetti, A. & Marks, T. J. Exploratory combustion synthesis: amorphous indium yttrium oxide for thin-film transistors. *J. Am. Chem. Soc.* **134,** 9593–9596 (2012).
64. Rim, Y. S., Lim, H. S. & Kim, H. J. Low-temperature metal-oxide thin-film transistors formed by directly photopatternable and combustible solution synthesis. *ACS Appl. Mater. Interfaces* **5,** 3565–3571 (2013).
65. Hennek, J. W. *et al.* Oxygen "getter" effects on microstructure and carrier transport in low temperature combustion-processed a-InXZnO (X = Ga, Sc, Y, La) transistors. *J. Am. Chem. Soc.* **135,** 10729–10741 (2013).
66. Smith, J. *et al.* Cation size effects on the electronic and structural properties of solution-processed In-X-O thin films. *Adv. Electron. Mater.* **1,** 1500146 (2015).
67. Jariwala, D. *et al.* Large-area, low-voltage, antiambipolar heterojunctions from solution-processed semiconductors. *Nano Lett.* **15,** 416–421 (2015).
68. Yu, X. *et al.* Spray-combustion synthesis: efficient solution route to high-performance oxide transistors. *Proc. Natl Acad. Sci. USA* **112,** 3217–3222 (2015).
69. Goldberger, J., Sirbuly, D. J., Law, M. & Yang, P. ZnO nanowire transistors. *J. Phys. Chem. B* **109,** 9–14 (2004).
70. Arnold, M. S., Avouris, P., Pan, Z. W. & Wang, Z. L. Field-effect transistors based on single semiconducting oxide nanobelts. *J. Phys. Chem. B* **107,** 659–663 (2002).
71. Ng, H. T. *et al.* Single crystal nanowire vertical surround-gate field-effect transistor. *Nano Lett.* **4,** 1247–1252 (2004).
72. Ju, S. *et al.* Fabrication of fully transparent nanowire transistors for transparent and flexible electronics. *Nature Nanotech.* **2,** 378–384 (2007).
73. Liao, L. *et al.* Multifunctional CuO nanowire devices: p-type field effect transistors and CO gas sensors. *Nanotechnology* **20,** 085203 (2009).
74. Sun, B. & Sirringhaus, H. Solution-processed zinc oxide field-effect transistors based on self-assembly of colloidal nanorods. *Nano Lett.* **5,** 2408–2413 (2005).
75. Ko, S. H. *et al.* ZnO nanowire network transistor fabrication on a polymer substrate by low-temperature, all-inorganic nanoparticle solution process. *Appl. Phys. Lett.* **92,** 154102 (2008).
76. Cho, S. Y. *et al.* Novel zinc oxide inks with zinc oxide nanoparticles for low-temperature, solution-processed thin-film transistors. *Chem. Mater.* **24,** 3517–3524 (2012).
77. Kawazoe, H. *et al.* P-type electrical conduction in transparent thin films of $CuAlO_2$. *Nature* **389,** 939–942 (1997).
78. Kudo, A., Yanagi, H., Hosono, H. & Kawazoe, H. $SrCu_2O_2$: a p-type conductive oxide with wide band gap. *Appl. Phys. Lett.* **73,** 220–222 (1998).
79. Kawazoe, H., Yanagi, H., Ueda, K. & Hosono, H. Transparent p-type conducting oxides: design and fabrication of p–n heterojunctions. *MRS Bull.* **25,** 28–36 (2000).
80. Chiu, T.-W., Tonooka, K. & Kikuchi, N. Fabrication of ZnO and CuCrO2:Mg thin films by pulsed laser deposition with *in situ* laser annealing and its application to oxide diodes. *Thin Solid Films* **516,** 5941–5947 (2008).
81. Gurlo, A., Bârsan, N., Ivanovskaya, M., Weimar, U. & Göpel, W. In_2O_3 and MoO_3–In_2O_3 thin film semiconductor sensors: interaction with NO_2 and O_3. *Sensor. Actuat. B-Chem.* **47,** 92–99 (1998).
82. Bai, S. *et al.* Preparation, characterization of WO_3–SnO_2 nanocomposites and their sensing properties for NO_2. *Sensor. Actuat. B-Chem.* **150,** 749–755 (2010).
83. Yuhas, B. D., Habas, S. E., Fakra, S. C. & Mokari, T. Probing compositional variation within hybrid nanostructures. *ACS Nano* **3,** 3369–3376 (2009).
84. Huang, H. *et al.* Low-temperature growth of SnO_2 nanorod arrays and tunable n–p–n sensing response of a ZnO/SnO_2 heterojunction for exclusive hydrogen sensors. *Adv. Funct. Mater.* **21,** 2680–2686 (2011).
85. Kim, K.-W. *et al.* The selective detection of C_2H_5OH using SnO_2–ZnO thin film gas sensors prepared by combinatorial solution deposition. *Sensor. Actuat. B-Chem.* **123,** 318–324 (2007).
86. Ivanovskaya, M., Kotsikau, D., Faglia, G. & Nelli, P. Influence of chemical composition and structural factors of Fe_2O_3/In_2O_3 sensors on their selectivity and sensitivity to ethanol. *Sensor. Actuat. B-Chem.* **96,** 498–503 (2003).
87. Cui, G., Zhang, M. & Zou, G. Resonant tunneling modulation in quasi-2D Cu_2O/SnO_2 p–n horizontal-multi-layer heterostructure for room temperature H_2S sensor application. *Sci. Rep.* **3,** 1–8 (2013).
88. Minami, T., Nishi, Y. & Miyata, T. High-Efficiency Cu_2O-based heterojunction solar cells fabricated using a Ga_2O_3 thin film as n-type layer. *Appl. Phys. Express* **6,** 044101 (2013).
89. Brittman, S. *et al.* Epitaxially aligned cuprous oxide nanowires for all-oxide, single-wire solar cells. *Nano Lett.* **14,** 4665–4670 (2014).
90. Akinaga, H. & Shima, H. Resistive random access memory (ReRAM) based on metal oxides. *Proc. IEEE* **98,** 2237–2251 (2010).
91. Lv, H. *et al.* Endurance enhancement of Cu-oxide based resistive switching memory with Al top electrode. *Appl. Phys. Lett.* **94,** 213502 (2009).
92. Lee, M.-J. *et al.* Electrical manipulation of nanofilaments in transition-metal oxides for resistance-based memory. *Nano Lett.* **9,** 1476–1481 (2009).
93. Sun, B. *et al.* Highly uniform resistive switching characteristics of TiN/ZrO_2/Pt memory devices. *J. Appl. Phys.* **105,** 061630 (2009).
94. Seo, J. W. *et al.* Transparent flexible resistive random access memory fabricated at room temperature. *Appl. Phys. Lett.* **95,** 133508 (2009).
95. Martins, R. *et al.* Write-erase and read paper memory transistor. *Appl. Phys. Lett.* **93,** 203501 (2008).
96. Watanabe, Y. Epitaxial all-perovskite ferroelectric field effect transistor with a memory retention. *Appl. Phys. Lett.* **66,** 1770–1772 (1995).
97. Baeg, K.-J. *et al.* Charge-trap flash-memory oxide transistors enabled by copper–zirconia composites. *Adv. Mater.* **26,** 7170–7177 (2014).
98. Nomura, K. *et al.* Subgap states in transparent amorphous oxide semiconductor, In-Ga-Zn–O, observed by bulk sensitive X-ray photoelectron spectroscopy. *Appl. Phys. Lett.* **92,** 202117 (2008).
99. Zhang, L. *et al.* Correlated metals as transparent conductors. *Nature Mater.* **15,** 204–210 (2016).
100. Choisnet, J., Bizo, L., Retoux, R. & Raveau, B. Antimony and antimony–tin doped indium oxide, IAO and IATO: promising transparent conductors. *Solid State Sci.* **6,** 1121–1123 (2004).
101. Makino, T. *et al.* Gallium concentration dependence of room-temperature near-band-edge luminescence in n-type ZnO:Ga. *Appl. Phys. Lett.* **85,** 759–761 (2004).
102. Servaites, J. D., Yeganeh, S., Marks, T. J. & Ratner, M. A. Efficiency enhancement in organic photovoltaic cells: consequences of optimizing series resistance. *Adv. Funct. Mater.* **20,** 97–104 (2010).
103. Wang, D. H., Kyaw, A. K. K., Gupta, V., Bazan, G. C. & Heeger, A. J. Enhanced efficiency parameters of solution-processable small-molecule solar cells depending on ITO sheet resistance. *Adv. Energ. Mater.* **3,** 1161–1165 (2013).
104. Minami, T. Present status of transparent conducting oxide thin-film development for indium-tin-oxide (ITO) substitutes. *Thin Solid Films* **516,** 5822–5828 (2008).
105. Liu, J., Hains, A. W., Wang, L. & Marks, T. J. Low-indium content bilayer transparent conducting oxide thin films as effective anodes in organic photovoltaic cells. *Thin Solid Films* **518,** 3694–3699 (2010).
106. Zhou, N. *et al.* Ultraflexible polymer solar cells using amorphous zinc-indium-tin oxide transparent electrodes. *Adv. Mater.* **26,** 1098–104 (2014).
107. Irwin, M. D., Buchholz, D. B., Hains, A. W., Chang, R. P. & Marks, T. J. P-type semiconducting nickel oxide as an efficiency-enhancing anode interfacial layer in polymer bulk-heterojunction solar cells. *Proc. Natl Acad. Sci. USA* **105,** 2783–2787 (2008).
108. Steirer, K. X. *et al.* Solution deposited NiO thin-films as hole transport layers in organic photovoltaics. *Org. Electron.* **11,** 1414–1418 (2010).
109. Berry, J. J. *et al.* Surface treatment of NiO hole transport layers for organic solar cells. *IEEE J. Sel. Top. Quant. Electron.* **16,** 1649–1655 (2010).
110. Zilberberg, K., Trost, S., Schmidt, H. & Riedl, T. Solution processed vanadium pentoxide as charge extraction layer for organic solar cells. *Adv. Energ. Mater.* **1,** 377–381 (2011).

© 2016 Macmillan Publishers Limited. All rights reserved

111. Shrotriya, V., Li, G., Yao, Y., Chu, C.-W. & Yang, Y. Transition metal oxides as the buffer layer for polymer photovoltaic cells. *Appl. Phys. Lett.* **88,** 073508 (2006).
112. Han, S. *et al.* Improving performance of organic solar cells using amorphous tungsten oxides as an interfacial buffer layer on transparent anodes. *Org. Electron.* **10,** 791–797 (2009).
113. Kröger, M. *et al.* Role of the deep-lying electronic states of MoO_3 in the enhancement of hole-injection in organic thin films. *Appl. Phys. Lett.* **95,** 123301 (2009).
114. Gwinner, M. C. *et al.* Doping of organic semiconductors using molybdenum trioxide: a quantitative time-dependent electrical and spectroscopic study. *Adv. Funct. Mater.* **21,** 1432–1441 (2011).
115. Stubhan, T. *et al.* High shunt resistance in polymer solar cells comprising a MoO_3 hole extraction layer processed from nanoparticle suspension. *Appl. Phys. Lett.* **98,** 253308 (2011).
116. Meyer, J., Khalandovsky, R., Görrn, P. & Kahn, A. MoO_3 Films spin-coated from a nanoparticle suspension for efficient hole-injection in organic electronics. *Adv. Mater.* **23,** 70–73 (2011).
117. Kim, J. Y. *et al.* New architecture for high-efficiency polymer photovoltaic cells using solution-based titanium oxide as an optical spacer. *Adv. Mater.* **18,** 572–576 (2006).
118. Steim, R., Kogler, F. R. & Brabec, C. J. Interface materials for organic solar cells. *J. Mater. Chem.* **20,** 2499–2512 (2010).
119. White, M. S., Olson, D. C., Shaheen, S. E., Kopidakis, N. & Ginley, D. S. Inverted bulk-heterojunction organic photovoltaic device using a solution-derived ZnO underlayer. *Appl. Phys. Lett.* **89,** 143517 (2006).
120. Law, M., Greene, L. E., Johnson, J. C., Saykally, R. & Yang, P. Nanowire dye-sensitized solar cells. *Nature Mater.* **4,** 455–459 (2005).
121. You, J. *et al.* A polymer tandem solar cell with 10.6% power conversion efficiency. *Nature Commun.* **4,** 1446 (2013).
122. Sun, Y., Seo, J. H., Takacs, C. J., Seifter, J. & Heeger, A. J. Inverted polymer solar cells integrated with a low-temperature-annealed sol-gel-derived ZnO film as an electron transport layer. *Adv. Mater.* **23,** 1679–1683 (2011).
123. Liao, H.-H., Chen, L.-M., Xu, Z., Li, G. & Yang, Y. Highly efficient inverted polymer solar cell by low temperature annealing of Cs_2CO_3 interlayer. *Appl. Phys. Lett.* **92,** 173303 (2008).
124. Lee, K. *et al.* Air-stable polymer electronic devices. *Adv. Mater.* **19,** 2445–2449 (2007).
125. Hau, S. K. *et al.* Air-stable inverted flexible polymer solar cells using zinc oxide nanoparticles as an electron selective layer. *Appl. Phys. Lett.* **92,** 253301 (2008).
126. Yusoff, A. R. b .M. *et al.* A high efficiency solution processed polymer inverted triple-junction solar cell exhibiting a power conversion efficiency of 11.83%. *Energy Environ. Sci.* **8,** 303–316 (2015).
127. Kyaw, A. K. K. *et al.* An inverted organic solar cell employing a sol-gel derived ZnO electron selective layer and thermal evaporated MoO_3 hole selective layer. *Appl. Phys. Lett.* **93,** 221107 (2008).
128. Bakke, J. R., Pickrahn, K. L., Brennan, T. P. & Bent, S. F. Nanoengineering and interfacial engineering of photovoltaics by atomic layer deposition. *Nanoscale* **3,** 3482–3508 (2011).
129. Wang, J.-C. *et al.* Highly efficient flexible inverted organic solar cells using atomic layer deposited ZnO as electron selective layer. *J. Mater. Chem.* **20,** 862–866 (2010).
130. Zhang, H. & Ouyang, J. High-performance inverted polymer solar cells with lead monoxide-modified indium tin oxides as the cathode. *Org. Electron.* **12,** 1864–1871 (2011).
131. Chen, C.-P., Chen, Y.-D. & Chuang, S.-C. High-performance and highly durable inverted organic photovoltaics embedding solution-processable vanadium oxides as an interfacial hole-transporting layer. *Adv. Mater.* **23,** 3859–3863 (2011).
132. Lin, M.-Y. *et al.* Sol–gel processed CuOx thin film as an anode interlayer for inverted polymer solar cells. *Org. Electron.* **11,** 1828–1834 (2010).
133. Leem, D.-S. *et al.* Efficient organic solar cells with solution-processed silver nanowire electrodes. *Adv. Mater.* **23,** 4371–4375 (2011).
134. Guo, F. *et al.* Fully printed organic tandem solar cells using solution-processed silver nanowires and opaque silver as charge collecting electrodes. *Energy Environ. Sci.* **8,** 1690–1697 (2015).

Acknowledgements

We thank the Northwestern University Materials Research Science and Engineering Center (NSF MRSEC DMR-1121262), ONR (MURI N00014-11-1-0690), AFOSR (FA 9550-08-1-0331) and Polyera Corp. for support of the Northwestern University research described here.

Additional information

Reprints and permissions information is available online at www.nature.com/reprints. Correspondence and requests for materials should be addressed to T.J.M and A.F.

Competing financial interests

The authors declare no competing financial interests.

© 2016 Macmillan Publishers Limited. All rights reserved